

Spatiotemporal Learning of Brain Dynamics from fMRI Using Frequency-Specific Multi-Band Attention for Cognitive and Psychiatric Applications

Sangyoon Bae¹, Junbeom Kwon², Shinjae Yoo³, Jiok Cha^{1,4,5*}

¹Interdisciplinary Program in Artificial Intelligence, Seoul National University, Gwanak-ro 1, Seoul, 08826, Seoul, South Korea.

²Department of Psychology, University of Texas at Austin, Dean Keeton Street, Austin, 78712, Texas, United States.

³Computational Science Initiative, Brookhaven National Laboratory, Brookhaven Avenue, Shirley, 11967, New York, United States.

⁴Department of Psychology, Seoul National University, Gwanak-ro 1, Seoul, 08826, Seoul, South Korea.

⁵Department of Brain and Cognitive Sciences, Seoul National University, Gwanak-ro 1, Seoul, 08826, Seoul, South Korea.

*Corresponding author(s). E-mail(s): connectome@snu.ac.kr;
Contributing authors: stellasybae@snu.ac.kr;

Abstract

A central challenge in neuroscience is understanding how the brain's complex nonlinear dynamics give rise to emergent properties underlying adaptive cognition and behavior across spatial and temporal scales. These dynamics exhibit scale-free and multifractal properties, shaping the adaptive reconfiguration of neural networks. However, conventional neuroimaging models remain constrained by assumptions of linearity and stationarity, limiting their capacity to fully characterize these intricate processes. Transformer-based architectures, known for capturing long-range dependencies in sequential data, naturally align with the brain's intrinsically hierarchical and temporal organization. Here, we introduce Multi-Band Brain Net (MBBN), a transformer-based deep learning framework that explicitly models frequency-specific spatiotemporal brain dynamics from fMRI by integrating scale-free network principles with frequency-resolved multi-band self-attention mechanisms.

Trained on three large-scale neuroimaging cohorts (UK Biobank, ABCD, ABIDE) totaling 45,951 individuals, MBBN reveals previously undetectable **frequency-dependent intrinsic network interactions**, shedding new light on distinct connectivity disruptions across psychiatric conditions (ADHD, ASD, depression). This extensive validation demonstrates robust generalizability and highlights core neural principles conserved across populations and developmental stages.

Specifically, MBBN achieves up to 30.59% higher predictive accuracy than state-of-the-art deep learning and conventional connectome-based methods, demonstrating the advantage of frequency-informed spatiotemporal modeling in capturing latent neural computations. Furthermore, MBBN’s attention-based interpretability reveals novel frequency-specific biomarkers for neurodevelopmental disorders, offering mechanistic insights into the hierarchical organization of brain function.

By providing a principled, interpretable framework for dissecting spatiotemporal learning mechanisms, MBBN advances methodological rigor and provides new insight into how dynamic neural computations underpin cognitive function and psychiatric vulnerability, with implications for brain decoding, cognitive neuroscience, and precision psychiatry.

Keywords: Spatiotemporal learning, Transformer, fMRI, Knowledge-guided Deep Neural Network, Neural Dynamics

1 Introduction

Understanding the brain’s dynamic processes is essential for unraveling the mechanisms underlying adaptive cognition and behavior. These processes influence critical functions such as learning, decision-making, and social interactions, and their dysregulation is closely linked to mental health conditions ([1–4]). While functional magnetic resonance imaging (fMRI) has been instrumental in probing brain activity, many conventional analytical methods remain constrained by assumptions of linearity, stationary, static connectivity. Approaches ranging from mass-univariate statistical tests and seed-based correlations to static functional connectivity maps often treat the brain as a relatively fixed system, thus failing to capture the temporal fluctuations, nonlinear interactions, and adaptive reconfigurations that characterize real neural dynamics. Recent advances in artificial intelligence (AI), particularly transformer-based architectures, have begun to address these shortcomings by modeling brain activity as a continuously evolving network of interdependent processes ([5–8]).

However, a critical gap remains in understanding and modeling two fundamental properties of neural dynamics: **scale-free dynamics** and **multifractal structures**. These properties are essential for comprehending the brain’s hierarchical complexity and adaptability ([2, 9, 10]). **Scale-free dynamics**, characterized by power-law relationships (Equation 1), reveal how neural activity maintains consistent patterns across different timescales and modalities. These dynamics play crucial roles in brain maturation and state transitions, with temporal variability serving as a key regulatory

mechanism ([11, 12]). The power-law exponent (β) varies across brain regions and states, providing valuable insights into neural network heterogeneity and serving as a potential marker for neurological and psychiatric disorders ([13, 14]).

Multifractality extends this framework by incorporating multiple scaling dimensions and power-law behaviors ([15–17]), offering a sophisticated approach to understanding the brain’s nested, hierarchical organization ([18, 19]). This property manifests in distinct frequency-dependent patterns that reflect neural adaptability and functional specialization ([20]). Evidence from fMRI, ECoG, and EEG studies suggests that these multifractal principles drive frequency-specific changes in connectivity and topological organization, particularly in properties such as small-worldness and modularity ([21, 22]). Understanding these patterns is crucial for developing more effective diagnostic and therapeutic strategies.

To address these challenges, we introduce the **Multi-Band Brain Net (MBBN)**, a novel framework based on Bidirectional Encoder Representations from Transformers (BERT) that integrates scale-free property-based frequency decomposition with advanced self-attention mechanisms and network theory concepts like communicability (Figure 1). MBBN divides fMRI BOLD signals into distinct frequency bands, enabling the capture of band-specific functional and topological properties. This approach provides a neurobiologically informed framework for modeling the brain’s multifractal and scale-free dynamics. The model features two key strengths: Firstly, its self-attention weighted connectivity dynamically models functional connectivity by capturing complex, **nonlinear interactions** and time-varying relationships between brain regions, thereby overcoming the limitations of traditional static, **correlation-based linear representations**. Secondly, a communicability-inspired pretraining loss function optimizes for biologically meaningful connectivity patterns. By leveraging these advances, MBBN not only provides deeper insights into brain function but also identifies frequency-specific markers for neurological and psychiatric disorders, offering a powerful new tool for clinical neuroscience research and applications.

$$\log(\text{power}) \propto -\beta \cdot \log(\text{frequency}) \quad (1)$$

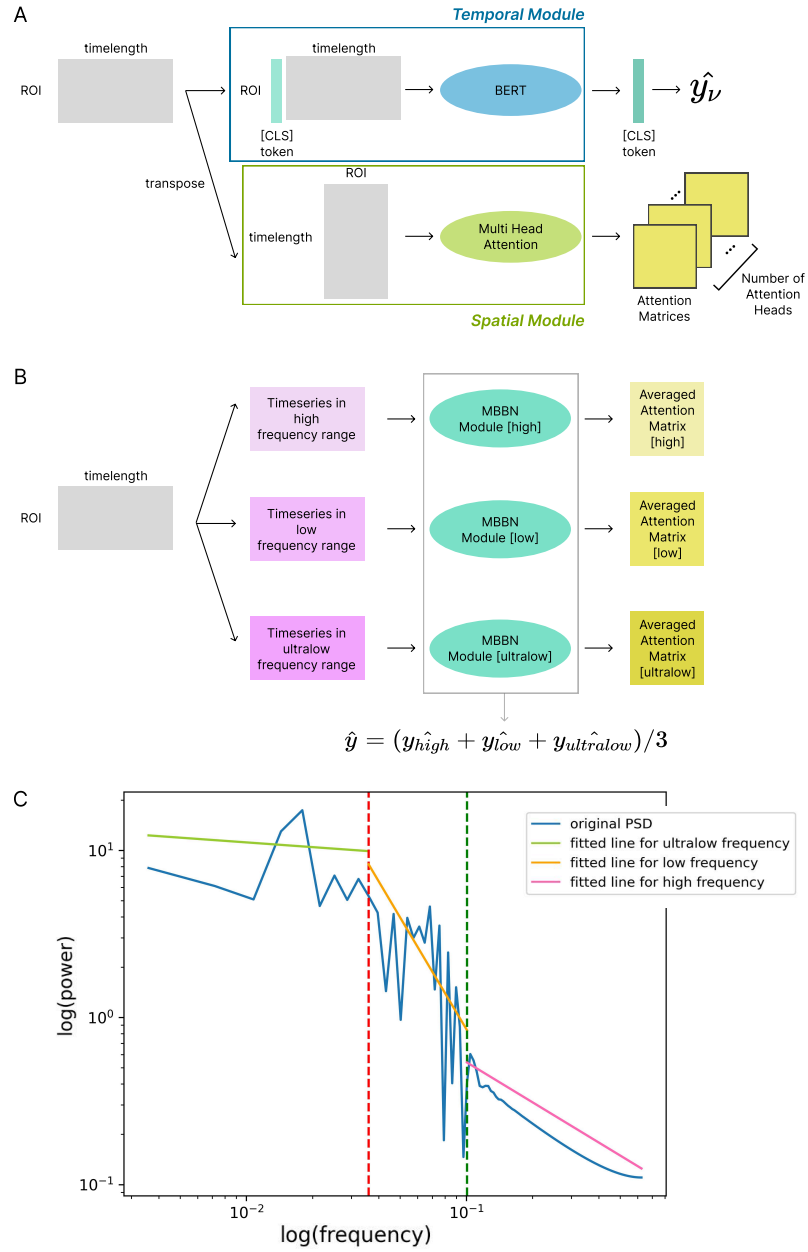


Fig. 1 Multi-Band Brain Net procedure

A. The MBBN module processes each timeseries signal, divided by frequency, within specific frequency ranges. In the temporal module (denoted as BERT), BERT updates the [CLS (Classification)] token, which is then passed through a classifier to generate a prediction \hat{y}_ν (ν represents the frequency range). The spatial module employs a multi-head attention mechanism to compute attention matrices representing the interactions between regions of interest (ROIs). **B.** The MBBN modules are applied to timeseries signals across three frequency ranges (ultra-low, low, and high frequency). Parameter sharing is implemented in the temporal module, while spatial modules have independent parameters for each frequency range. The final output of MBBN is computed as the average of the predictions across all frequency ranges, along with attention matrices specific to each frequency range. **C.** The frequency decomposition process is demonstrated using a representative sample from the UKB dataset. Although the knee frequencies (f_1 , f_2) may vary across individuals, the overall pattern of frequency division remains consistent. The blue line represents the original power spectral density (PSD) of the fMRI signal. The pink, yellow-green, and yellow lines show the fitted power-law functions for the high, ultra-low, and low-frequency ranges, respectively. The dotted red and green lines indicate the frequency boundaries: ultra-low to low (f_1), and low to high (f_2) frequencies, respectively.

2 Results

2.1 Comparison of Model Performance Across Various Downstream Tasks

To evaluate model performance, we trained MBBN from scratch on multiple downstream tasks spanning biological, cognitive, and clinical domains, using both the HCP-MMP1 and Schaefer atlases across the UKB and ABCD datasets. MBBN consistently outperformed baseline models across all tasks. For biological phenotype prediction (sex classification), MBBN achieved notable gains of up to 11.6% on UKB and 18.88% on ABCD using the HCP-MMP1 atlas, with similar improvements using the Schaefer atlas (9.06% on UKB, 14.78% on ABCD). In cognitive assessment tasks, fluid intelligence prediction showed substantial improvements on the ABCD dataset (up to 18.88% with HCP-MMP1, 8.03% with Schaefer). For clinical applications, depression prediction on the UKB dataset demonstrated meaningful gains (up to 9.42% with HCP-MMP1, 6.98% with Schaefer). Comprehensive performance comparisons, including task-specific metrics and statistical analyses, are detailed in Appendix.

2.2 Communicability-based masking loss improves fine-tuning performance over random masking loss.

A key component of our methodology was a pretraining loss function designed to mask nodes with high communicability within the brain network. This strategy was predicated on the hypothesis that selectively reconstructing these highly influential nodes during pretraining would better represent the complex communication patterns within the brain. To validate this hypothesis and evaluate the downstream impact of this pretraining strategy, MBBN was subsequently fine-tuned on two clinically relevant classification tasks: ADHD classification using the ABCD dataset, and ASD classification using the ABIDE dataset. These datasets and tasks were chosen for their established clinical significance and high prevalence rates.

Fine-tuning experiments revealed a clear advantage for the *MBBN-high* model, which employed a pretraining strategy that selectively masked nodes with high communicability. This approach resulted in significant performance improvements compared to baselines: a 5.55% gain in ADHD classification accuracy and a remarkable 30.59% gain in ASD classification accuracy. In contrast, models using random node masking (*MBBN-random*) or masking nodes with low communicability (*MBBN-low*) showed inferior performance, even compared to the MBBN model trained from scratch (*MBBN-from scratch*). These findings underscore the critical role of communicability-based pretraining in effectively leveraging the underlying network structure of the data to enhance predictive performance. Complete results and statistical details are available in Appendix.

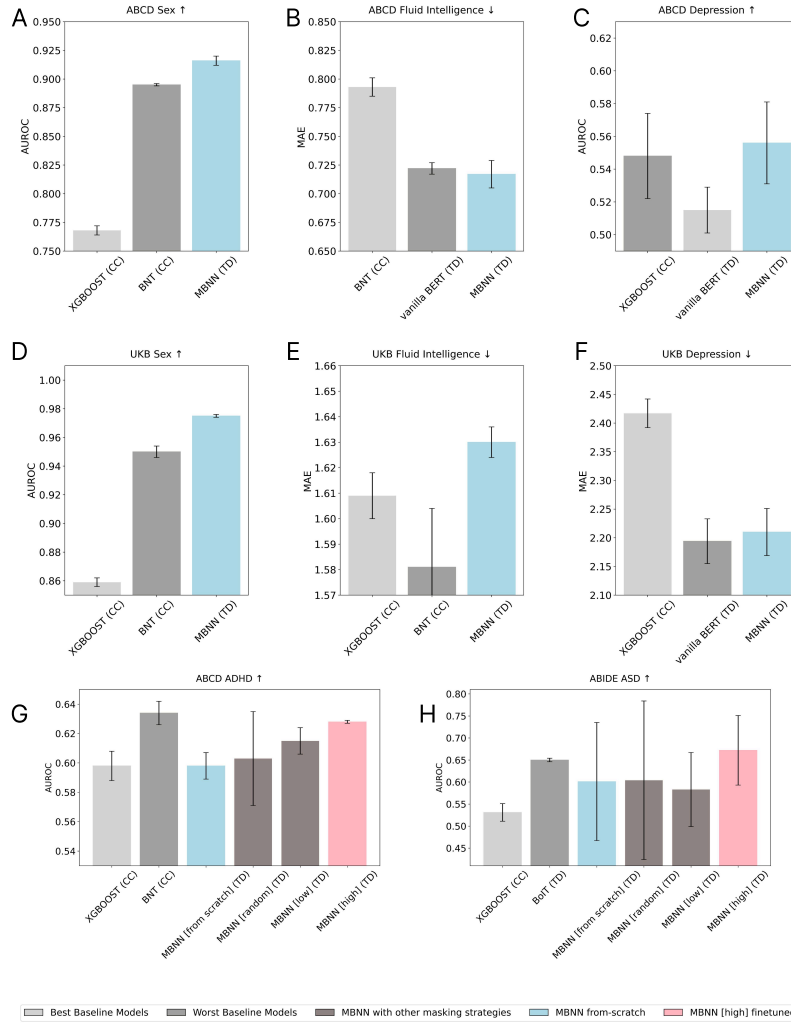


Fig. 2 Comparative Analysis of fMRI Prediction Models. Across datasets and tasks, the proposed MBNN demonstrates superior predictive performance compared to baseline models including state-of-the-art models in the field (e.g., Brain Network Transformer ([5])), as well as vanilla BERT (without multi-fractality division). [CC] indicates models based on Pearson’s correlation-based connectivity; [TD] represents, models accounting for temporal dynamics. The x-axis denotes the models, and the y-axis represents performance metrics, with AUROC used for classification tasks and MAE for regression tasks. (A–B) show results for sex prediction, (C–D) for fluid intelligence prediction, (E–F) for depression prediction, G for ADHD prediction, and H for ASD prediction. Specifically: (A, B, C, G) correspond to the ABCD dataset using the HCP-MMP1 atlas. (D, E, F) correspond to the UKB dataset using the HCP-MMP1 atlas. H correspond to the ABIDE dataset using the HCP-MMP1 atlas.

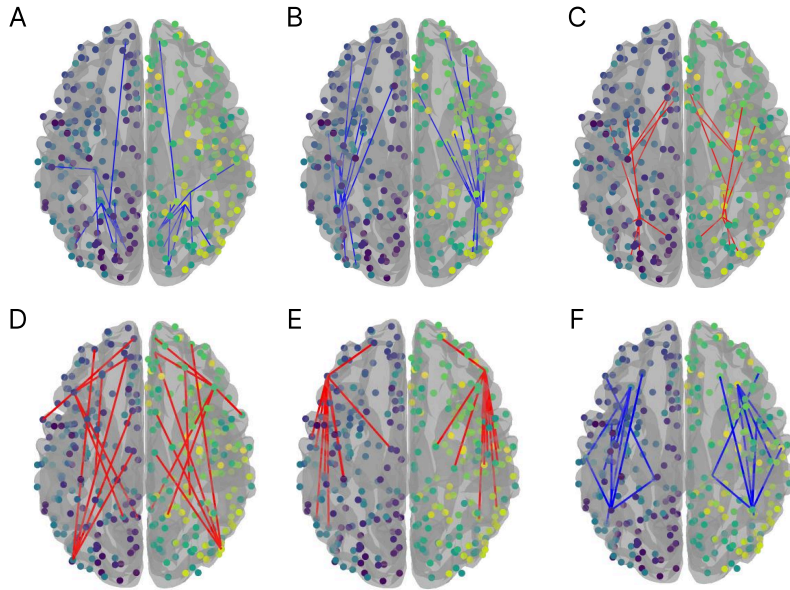


Fig. 3 Self-Attention-Based Connectivity Learned from Resting fMRI Distinguishing ADHD and ASD from Healthy Controls. For presentational purposes, this figure highlights statistically significant connections with the top 10 largest effect sizes that differentiate individuals with ADHD (A-C) or ASD (D-F) from healthy controls (HC) (FDR corrected P 's ≤ 0.05). [Red: Higher in the disorder group; Blue: Lower in the disorder group.]. A detailed list of the top 100 connectivity is provided in the Appendix F. (A-C) show ADHD connectivity patterns compared to HC across frequency bands: high (A), low (B), and ultralow (C). (D-F) illustrate ASD patterns compared to HC: high (D), low (E), and ultralow (F). The HCP-MMP1 atlas was used.

2.3 Key connectivity for mental illness classification revealed by attention mechanisms

We utilized a Grad-CAM-based attribution score to identify self-attention-weighted-connectivity with large effect sizes distinguishing healthy controls from individuals with mental illness and analyzed their roles. Details are described in Section 3.9.

In the ABCD test dataset (HCP-MMP1 atlas), frequency-dependent differences in functional connectivity patterns were identified between the ADHD and HC groups. ADHD showed reduced connectivity in high and low frequencies, while exhibiting increased connectivity in the ultralow-frequency range (Figure 3). These findings reveal frequency-specific neural connectivity alterations in ADHD. The results of the t-test distinguishing between the HC and ADHD groups showed that 6.55% of the statistically significant connections ($p < 0.05$) were in the high-frequency range, with the 75% quantile value of Cohen's d score being 0.71. In contrast, the low-frequency range accounted for only 1.67%, with the 75% quantile value of Cohen's d being 0.17. The ultralow frequency range accounted for 8.39%, with the 75% quantile value of Cohen's d being 0.71.

In the high-frequency range (Figure 3 A), distinct connectivity patterns emerged involving key regions such as ParaHippocampal Area 3 and VentroMedial Visual Area,

highlighting potential disruptions in visual processing and memory formation. Similarly, the low-frequency range (Figure 3 B) showed significant differences centered around Area PH (Parahippocampal Area) and Primary Auditory Cortex, pointing to altered neural system how sound information is integrated and processed in memory. In the ultralow-frequency range (Figure 3 C), connectivity changes in VentroMedial Visual Area 3 and Area TF suggest impairments related to visual processing and attention regulation.

In the ABIDE test dataset (HCP-MMP1 atlas), the results of the t-test distinguishing between the HC and ASD groups showed that 7.88% of the statistically significant connections ($p < 0.05$) were in the high-frequency range, with the 75% quantile value of Cohen’s d score being 1.19. In contrast, the low-frequency range accounted for only 0.24%, with the 75% quantile value of Cohen’s d being 0.74. The ultralow frequency range accounted for 0.91%, with the 75% quantile value of Cohen’s d being 0.84.

ASD-related connectivity patterns exhibited localized differences compared to healthy controls (HC), with varying effects across frequency ranges (Figure 3). In the high-frequency range (Figure 3 D), connectivity differences were observed in regions such as PGi (PG inferior) and 47m (Area 47 medial), potentially linked to challenges in socio-emotional and executive functions. In the low-frequency range (Figure 3 E), IFSa showed prominent differences, indicating possible impairments in executive and communication functions. Finally, in the ultralow-frequency range (Figure 3 F), connectivity alterations in Lateral Area 7P and the Insular Granular Complex suggest disruptions in sensory and emotional processing.

In both the ABCD and ABIDE datasets, analysis of false positive and false negative subjects (based on predicted values) showed no statistically significant connections in the self-attention-based connectivity analysis.

3 Methods

3.1 Preprocessing

The ABCD, UKB, and ABIDE datasets underwent initial preprocessing prior to analysis. In the ABCD study, a bandpass filter ranging from 0.009 to 0.08 Hz was applied to harmonize multi-site data [23]. In the UKB study, a bandpass filter ranging from 0.008 to 0.1 Hz was used to minimize the effects of heart rate variability and hemodynamic response delays [24]. In the ABIDE study, a finite impulse response (FIR) filter with a passband of 0.01–0.1 Hz [25] was employed to facilitate multi-site data integration. For the present study, additional preprocessing was performed on the resting-state BOLD data. The following preprocessing procedures were applied to each participant’s resting-state BOLD data: First, skull-stripping, slice-timing correction, and spatial normalization to MNI space were conducted using fMRIPrep ([26]). Subsequently, head motion artifacts and signals from white matter were removed using component-based noise correction (CompCor) [27]. The mean time-series signals from predefined regions of interest (ROIs) were extracted using the Nilearn package, with HCP-MMP1 symmetric ([28]) and Schaefer 400 ([29]) atlases employed for ROI definitions. Participants whose data contained voxels with NaN values, typically arising

from the regression of unreliable white-matter signals, were excluded from the analysis. Additionally, to minimize spurious signal fluctuations due to scanner instability, the first 20 volumes of each time-series were discarded.

For deep neural network training, uniform sequence lengths across all participants were required. To standardize the sequence length, it was set to the smallest multiple of 8 that was greater than or equal to the shortest sequence length in the dataset, optimizing computational efficiency for GPU-based matrix operations. The final sequence lengths for the datasets were as follows: UK Biobank (UKB) 464, Adolescent Brain Cognitive Development (ABCD) 348, and Autism Brain Imaging Data Exchange (ABIDE) 280.

3.2 Dataset

Demographic and diagnosis distribution details for the three datasets (UKB, ABCD, ABIDE) are summarized in Table 1. The UK Biobank (UKB) dataset, which includes 41,283 participants, was used for pretraining due to its large sample size and broad demographic representation. This extensive dataset enabled the model to capture generalizable brain dynamics patterns. The Adolescent Brain Cognitive Development (ABCD) dataset, consisting of 4,527 participants (including individuals with ADHD and healthy controls), and the Autism Brain Imaging Data Exchange (ABIDE) dataset, which includes 141 participants (comprising individuals with ASD and healthy controls), were employed for fine-tuning to capture disorder-specific patterns.

ADHD diagnosis was based on CBCL attention and ADHD scores exceeding a T-score threshold of 65, while healthy controls were defined as individuals with no diagnosed mental health disorders ([30]). This classification ensured a distinct separation between clinical and non-clinical groups, facilitating model training and evaluation.

Features	UKB	ABCD	ABIDE
Gender (M/F)	40,699 (21,556/19,143)	8,896 (4,662/4,234)	141 (114/27)
Age (year)	54.9±7.5	-	14.3±3.6
Age (month)	-	119.2±7.5	-
Depression (ph9 score)	11.5±3.5	-	-
Diagnosis (disorder/controls)	-	141 (77/64)	-
Fluid intelligence (z-score)	-	0.01±0.91	-

Table 1 Features of the UKB, ABCD, and ABIDE subjects. Disorder denotes ADHD in the ABCD dataset and ASD in the ABIDE dataset.

3.3 Experimental Settings

To address the imbalance in clinical variables within the dataset, stratified sampling was employed to ensure balanced distributions of target variables (ADHD, depression, ASD) across the training, validation, and test sets. A similar approach was used for the biological phenotype (sex), which showed minimal imbalance. To enhance model robustness and reduce overfitting, training was conducted using three random seeds, and the average performance across these runs was reported.

Gradient clipping with a norm of one and gradient accumulation were applied to stabilize training and improve predictive accuracy. To accelerate the training process, Automatic Mixed Precision (AMP) was utilized. The BERT model architecture comprised 8 hidden layers and 8 or 12 attention heads, depending on the number of regions of interest (ROIs) in the atlas used. The number of attention heads was chosen based on the constraint that it should be a divisor of the total number of ROIs. Hyperparameter optimization included testing learning rates ([1e-5, 1e-2]), weight decay ([1e-3, 1e-2]), learning rate policy (step, SGDR), and optimizers (Adam, AdamW, RMSprop).

For computational efficiency, pretraining was performed on a single A100 GPU, while training from scratch and fine-tuning were conducted using a single NVIDIA RTX 3090 GPU. The number of epochs was set to 100 for training from scratch. Efficient pretraining was achieved by determining the optimal number of epochs using weightwatcher ([31]), which identifies well-trained layers based on statistical learning theory. Optimal pretraining epochs were set to 1,000 for the HCP-MMP1 atlas and 400 for the Schaefer 400 atlas. Additional methodological details are provided in Appendix A.2.

3.4 Dividing frequencies

3.4.1 Frequency Dividing Strategy

$$Power(f) = \frac{A \cdot f_1^2}{f^2 + f_1^2} \quad (2)$$

Let $w(f)$ be defined as:

$$w(f) = \begin{cases} 0 & \text{if } \log(f) < \log(f_2) - s \\ 1 & \text{if } \log(f) > \log(f_2) + s \\ \frac{1}{2}(1 - \cos(\frac{\pi(\log(f) - \log(f_2) + s)}{2s})) & \text{otherwise} \end{cases} \quad (3)$$

Then the spline multifractal function is:

$$Power(f) = A \cdot f^{\beta_{low}(1-w(f)) + \beta_{high}w(f)} \quad (4)$$

where:

- A is the amplitude.
- β_{low} is the low-frequency scaling exponent.
- β_{high} is the high-frequency scaling exponent.
- f_2 is the knee frequency.
- s is the smoothness parameter.

To segment the resting-state fMRI data into distinct frequency bands, we applied both Lorentzian and spline multifractal equations to the power spectral density (PSD). These methods allowed us to identify knee frequencies (f_1 , f_2) that demarcate the transitions between frequency bands and reveal their scale-free properties. The Lorentzian equation (Equation 2) was used to estimate f_1 , the first knee frequency, by fitting the entire PSD. For frequencies above f_1 , the spline multifractal equation (Equation 4)

was applied to identify f_2 , the second knee frequency. To ensure a smooth transition between different frequency regimes, we implemented cubic spline smoothing in the multifractal equation, preventing artifacts that could arise from abrupt transitions at the knee frequencies. The smoothing weight was adapted based on methodologies from ([32, 33]). The transition function $w(f)$ plays a crucial role in interpolating between two distinct power-law regimes. When $x \ll f_2$, $w(f) \approx 0$, ensuring that the function follows the lower-frequency power-law behavior characterized by β_{low} . Conversely, when $x \gg f_2$, $w(f) \approx 1$, shifting the function to the higher-frequency power-law behavior defined by β_{high} . In the intermediate range, $w(f)$ smoothly transitions between these regimes, with the parameter s controlling the sharpness of the transition. This formulation enables a continuous and differentiable shift between scaling regimes while preserving the structural properties of the signal. These knee frequencies were used to segment the time-series data into three frequency bands: ultra-low frequency (below f_1), low frequency (between f_1 and f_2), and high frequency (above f_2). The segmentation process was implemented using the Finite impulse response (FIR) and Boxcar filter from the *nitime* package. The optimal filter types (FIR and Boxcar) were determined through systematic hyperparameter tuning on validation sets, evaluating their performance impact on the overall model. The Lorentzian function, having only two parameters, was efficiently fitted using the curve fit function from the SciPy package, which is well-suited for low-dimensional fitting. In contrast, the spline multifractal function, which involves five parameters, was fitted using the *iminuit* package, which is optimized for high-dimensional parameter estimation. In all three datasets, ANOVA analysis of f_1 and f_2 computed separately for each dataset, revealed a statistically significant difference between the two values ($p < 0.001$), indicating that f_1 and f_2 reflect distinct frequency characteristics.

To assess the scale-free properties of these frequency bands, we computed β values for each range, as shown in Equation 1. The results, summarized in Table 3, demonstrated significant differences in β values across bands ($p < 0.001$), supporting the hypothesis that each frequency component exhibits distinct scale-free dynamics. These results highlight that different frequency bands in the brain exhibit unique functional and topological properties. Specifically, lower frequencies are associated with long-range, global integration of brain activity, while higher frequencies correspond to more localized processing and rapid adaptation ([34, 35]). This finding reinforces the concept of multifractal behavior in brain signals, which has been previously observed in ECoG and EEG recordings ([20]). These β values, denoted as β_{ultralow} , β_{low} , β_{high} , correspond to the ultra-low, low, and high-frequency bands, respectively.

3.4.2 Frequency Division and Physiological Relevance

The values of f_1 and f_2 varied slightly across datasets (Table 2), yet consistently fell within specific ranges, reinforcing their physiological relevance. f_1 (0.046 Hz for ABCD, 0.062 Hz UKB datasets, and 0.018 Hz for ABIDE) corresponds to the time constant of an exponentially decaying function ([36]). Meanwhile, f_2 marks the transition to higher-frequency brain processes. f_2 was 0.078Hz for ABCD, 0.096Hz for UKB, and 0.030Hz for ABIDE. In ABCD and UKB, the f_2 values approaches the upper bound of conventional resting-state fMRI bandpass filtering (0.009-0.08Hz for

ABCD, 0.008-0.1Hz for UKB). However, contemporary fMRI preprocessing pipelines commonly employ the Butterworth filter, which applies a gradual roll-off rather than an abrupt cutoff at upper bound (0.08Hz for ABCD, 0.1 Hz for UKB). This design minimizes phase distortion while effectively suppressing physiological noise from respiratory and cardiac ([37]). Consequently, the proximity of f_2 to upper bound of bandpass filtering does not imply a loss of meaningful higher-frequency information, as these signals are gradually attenuated rather than completely eliminated.

The significant differences in β values across frequency bands further validate the frequency-dependent multifractal properties of fMRI signals. This demonstrates the potential of frequency-specific analyses to uncover multi-scale brain network organization and adaptive complexity in brain activity. Additionally, the reliability of f_1 and f_2 across different datasets emphasizes the generalizability of this approach, making it a powerful tool for further research into brain dynamics.

Dataset	f_1	f_2
ABCD	0.0456 \pm 0.0106	0.0784 \pm 0.0151
UKB	0.0624 \pm 0.0113	0.0961 \pm 0.0157
ABIDE	0.0182 \pm 0.0121	0.0299 \pm 0.0256

Table 2 Different f_1 and f_2 among datasets

Dataset	$\beta_{ultralow}$	β_{low}	β_{high}
ABCD	0.2442 \pm 0.2991	1.7845 \pm 0.3836	1.1595 \pm 0.4260
UKB	0.0209 \pm 0.2185	2.8959 \pm 0.4562	1.1232 \pm 0.4107
ABIDE	0.5805 \pm 0.3925	2.5939 \pm 0.3923	0.9563 \pm 0.2228

Table 3 Different β value among frequency ranges and datasets

The spline multifractal equation and the Lorentzian equation showed superior fitting performance across all datasets as depicted in Table 4. The consistent and high goodness-of-fit metrics across different datasets ($R^2 > 0.66$ for all cases) demonstrate the effectiveness of our dual-equation fitting approach, validating its reliability for characterizing the frequency-domain properties of resting-state fMRI data.

3.5 Model Design

3.5.1 Model Architecture

Our model consists of two primary modules: the temporal module and the spatial module. These modules work synergistically to encode both the temporal and spatial characteristics of frequency-divided timeseries data, as shown in Figure 1 A. To ensure an effective balance between generalization and specificity, a parameter-sharing strategy is employed, as outlined below.

Dataset	Lorentzian Equation	Spline Multifractal Equation
	Mean R^2	Mean R^2
ABCD	0.7423 \pm 0.0765	0.6822 \pm 0.2375
UKB	0.6605 \pm 0.0786	0.8292 \pm 0.0854
ABIDE	0.7435 \pm 0.1018	0.8309 \pm 0.1019

Table 4 Goodness of Fit (R^2) Statistics for Lorentzian and Spline Multifractal Equations Across Datasets

Note: Values are presented as mean \pm standard deviation. R^2 values indicate the proportion of variance explained by each model.

The temporal module (depicted as a blue oval in Figure 1 A) is designed to capture the temporal dynamics of the data. For each frequency-divided timeseries (ultra-low, low, and high), the data are processed independently using a shared BERT encoder, reflecting the temporal similarities across frequency bands. The BERT encoder outputs a sequence of hidden states for each timeseries, with the final hidden state corresponding to the [CLS] token passed to a classifier. This process produces logits ($y_{\hat{ultra}low}$, $y_{\hat{low}}$, and $y_{\hat{high}}$), which represent the model’s predictions for each frequency range. The hidden dimension size of the MBBN temporal module is set to match the number of ROIs. Due to the constraints imposed by the BERT backbone in MBBN, the number of attention heads must be a divisor of the hidden dimension size. Consequently, when using the Schaefer atlas, the number of attention heads is set to 8, whereas for the HCP MMP1 atlas, it is set to 12.

The spatial module (depicted as a yellow-green oval in Figure 1 A) focuses on the spatial connectivity among regions of interest (ROIs). Unlike the temporal module, the spatial module uses a frequency-specific approach to capture the distinct spatial patterns of each frequency band. Specifically, a multi-head attention mechanism is applied to the transposed timeseries data, generating a set of attention matrices for each frequency band. These attention matrices—reflecting the distinct focus of different heads—are averaged to produce a single attention matrix per band. These averaged matrices represent the spatial connectivity patterns, which are subsequently used to compute the spatial loss (Equation 9). In practice, the MBBN spatial module receives the transposed input of the temporal module, so the number of attention heads must divide the sequence length. For example, we set 12 heads for ABCD (sequence length is 348) and 8 heads for both UKB (464) and ABIDE (280).

Although the temporal and spatial modules do not directly exchange hidden states, they remain closely coupled through the composite loss function. The total loss combines cross-entropy (or task-specific) loss with the spatial loss, so backpropagation updates parameters across the entire network. As a result, while the BERT-based temporal module primarily absorbs gradient updates from the mask and task objectives, and the attention-based spatial module is mostly driven by spatial loss, their optimization processes are fundamentally interdependent. Changes in one module can indirectly shift the parameter landscape of the other, ensuring a shared optimization of temporal and spatial patterns.

This architectural design supports module specialization—BERT focuses on temporal dependencies, while the attention module models spatial relationships—without direct interference. Yet both modules ultimately contribute to the network’s overall optimization, facilitating a more integrated representation of brain dynamics. Additionally, by treating these modules as partly separable, the framework allows for independent evaluation and targeted enhancements in each module, preserving their complementary roles in the final model.

As shown in Figure 1 B, the temporal and spatial modules operate on each frequency range, generating corresponding logits and attention matrices. To obtain the final prediction, the logits from the three frequency ranges are averaged and compared with the true label (y_{true}) using a task-specific loss function ($Loss_{task}$). In parallel, a spatial loss is computed to enforce distinct spatial connectivity patterns across frequency bands. The total loss function, which combines these two components, is defined as:

$$Loss_{total} = Loss_{task}(y_{true}, \frac{y_{ultralow} + y_{low} + y_{high}}{3}) + \lambda \cdot Loss_{spatial} \quad (5)$$

In Equation 5, $Loss_{task}$ represents the cross-entropy loss for classification tasks or L1 loss for regression tasks. The $Loss_{spatial}$ term, as described in Section 9, emphasizes the distinct spatial connectivity patterns inherent to each frequency band. λ was determined by hyperparameter tuning. The chosen λ value and the filter type (described in Section 3.4.1) were shown in Table 5.

Dataset	Filter Type	Spatial Factor λ
<i>Schaefer atlas</i>		
ABCD	Boxcar	10
UKB	Boxcar	1
ABIDE	Boxcar	100
<i>HCPMMP1 atlas</i>		
ABCD	FIR	10
UKB	Boxcar	1
ABIDE	Boxcar	100

Table 5 Optimal filter types and λ determined through hyperparameter tuning

3.5.2 Parameter Sharing

To enhance model performance, we adopted a multi-view learning approach, which is well-suited for frequency-divided timeseries data. We treat the ultra-low, low, and high frequency time series as three ‘views’ of the same underlying data, where different representations of the same underlying phenomenon are considered. Multi-view data enables the model to leverage shared information across views, allowing it to capture complementary aspects of the data.

For the temporal module, we utilized a parameter-sharing strategy. Given that temporal dynamics exhibited minimal differences across frequency bands (as indicated

by similar autocorrelation structures), a single shared BERT encoder was used to process timeseries data from all frequency bands. This approach allows the model to exploit common temporal patterns across frequency bands, leading to a robust and generalized representation of temporal dynamics.

In contrast, the spatial module required a frequency-specific approach. Previous studies ([38]) and our analysis have shown that spatial connectivity patterns differ significantly across frequency bands. Therefore, we implemented frequency-specific parameters for the spatial module. Self-attention-weighted connectivity was calculated independently for each frequency range, with each frequency band using its own set of parameters to capture the unique spatial relationships among ROIs. This design ensures that the model preserves the distinct connectivity characteristics of each frequency band while maintaining the interpretability of spatial attention.

This parameter-sharing strategy strikes a balance between generalization and specificity. Shared temporal parameters capture global patterns common across frequency bands, while frequency-specific spatial parameters emphasize the unique spatial relationships within each frequency band. By integrating this approach with task-specific and spatial loss functions (Equation 5), the model effectively captures the multi-level organization of frequency-divided timeseries data, facilitating the identification of relevant biomarkers across multiple scales.

3.6 Temporal BERT Module

3.6.1 Data Encoding

To capture temporal dependencies across regions of interest (ROIs), the frequency-divided time-series data were sequentially input into the BERT model. Each signal at a single time point was treated as a distinct token, with the token length corresponding to the total number of ROIs. This encoding strategy effectively represented both the temporal and spatial dynamics of the fMRI data, ensuring that these features were preserved for downstream analysis.

3.6.2 Using Original Form of BERT

fMRI BOLD signal data consists of long sequences, typically ranging from 280 to 464 tokens, necessitating a model that can handle such extended sequences. BERT, originally developed for natural language processing (NLP) tasks, is particularly well-suited for this purpose due to its ability to capture complex contextual relationships within sequences ([39]). This makes BERT an ideal model for modeling the intricate temporal dependencies inherent in fMRI data.

In contrast, models like GPT are optimized for text generation tasks and do not emphasize inter-sequence contextual relationships, which are critical for our analysis. Unlike GPT’s causal masking—which is tailored to text generation and unidirectional context—BERT’s bidirectional attention allows it to capture long-range temporal dependencies from both past and future time points simultaneously, making it more suitable for modeling complex fMRI time series. Although some previous studies have used convolutional filters as a preprocessing step before entering signals into BERT ([40]), we chose to bypass this step. Although convolutional preprocessing can be

computationally efficient, it may sacrifice the preservation of fine-grained temporal dynamics within the fMRI data, which could impact model performance (see Appendix D). By directly inputting the time-series data into the original BERT structure, we aimed to retain the full complexity of the temporal dynamics, allowing the model to effectively capture both short-term and long-term dependencies.

3.7 Spatial Attention Module

3.7.1 Self-Attention-Weighted Connectivity

Traditional methods of functional connectivity based on statistical correlations assume linear relationships and static connectivity ([41]). However, these approaches do not account for the nonlinear and time-varying nature of brain connectivity. To address this limitation, we employed a dynamic method that captures the complex, evolving interactions within resting-state functional networks. This method provides a more accurate representation of the diverse and temporal relationships among brain regions.

Given that spatial connectivity reflects the relationships between brain regions, we hypothesized that a self-attention mechanism, as used in transformer models ([42]), would be a suitable alternative. Self-attention mechanisms are designed to capture relationships between tokens (or regions, in our case), and the attention matrices they generate are diverse, reflecting the multifaceted nature of these relationships. While self-attention with multiple parallel attention heads is referred to as multi-head attention, our implementation specifically employed the multi-head attention mechanism to capture diverse representational information simultaneously. Multi-head attention mechanisms allow neural networks to focus on different aspects of input data simultaneously, similar to how different neural circuits in the brain can process the same sensory information through specialized pathways. In this approach, the input is projected into multiple representation spaces where separate attention computations occur in parallel, enabling the model to capture diverse relationships within the data. This parallel processing architecture has proven remarkably effective for complex tasks like language understanding, where different heads can specialize in detecting various linguistic patterns such as syntactic relationships, semantic connections, or long-range dependencies. In our transformer model architecture, multiple attention heads are employed, with each head generating its own $N_{ROI} \times N_{ROI}$ attention matrix, where N_{ROI} denotes number of ROIs. These attention matrices differ across heads as each head learns to capture different aspects of the relationships between ROIs. For example, one head might focus more strongly on frontal-temporal relationships while another might emphasize occipital-parietal connections. The final attention-based connectivity is then computed by averaging these head-specific attention matrices. To more effectively capture the complex dynamic relationships between ROIs compared to traditional correlation-based methods, we defined self-attention-weighted connectivity as the mean of the attention matrices ($Attention\ matrix \in \mathbb{R}^{(N_{ROI} \times N_{ROI})}$), where each matrix represents an estimate of spatial connectivity between ROIs.

3.7.2 Spatial Loss

The three frequency-divided components, separated by frequencies (f_1, f_2), exhibit more distinct differences in connectivity patterns ([38]). To highlight these differences, we introduced a spatial loss term designed to encourage different spatial connectivity patterns for each frequency range. Specifically, the loss term maximizes the sum of L1 losses between attention matrices derived from different frequency ranges (Equation 9). The use of the negative logarithm in the loss function magnifies smaller differences between frequency bands, ensuring that even subtle distinctions are emphasized during training. This approach enables the model to learn unique spatial connectivity patterns for each frequency band, reflecting the potentially distinct contributions of these bands to brain activity. Moreover, this spatial loss term works in conjunction with other loss functions in the model to strike a balance between generalization and specificity.

$$Loss_{high-low} = Loss_{L1}(attmat_{high}, attmat_{low}) \quad (6)$$

$$Loss_{high-ultralow} = Loss_{L1}(attmat_{high}, attmat_{ultralow}) \quad (7)$$

$$Loss_{ultralow-low} = Loss_{L1}(attmat_{ultralow}, attmat_{low}) \quad (8)$$

$$Loss_{spatial} = -\log(Loss_{high-low} + Loss_{high-ultralow} + Loss_{ultralow-low}) \quad (9)$$

3.8 Pretraining Strategy Based on Communicability

3.8.1 Masking Strategy and Pretraining Loss

The goal of pretraining is to enable the model to learn the underlying structure of brain signal data in a self-supervised manner. To achieve this, we incorporated the concept of communicability into the pretraining process. A detailed definition of communicability used in this study is provided in Appendix A.1.

Our pretraining strategy draws inspiration from masking techniques commonly used in language models to capture contextual relationships and data patterns ([39]). We hypothesized that masking nodes with high communicability would encourage the model to infer the activity of these influential nodes based on the surrounding network dynamics. This approach highlights the role of high-communicability hubs in shaping the overall structure of resting-state networks.

To validate this hypothesis, we compared three masking strategies:

- Masking nodes with high communicability.
- Masking nodes with low communicability.
- Randomly masking regions of interest (ROIs).

Detailed model performance results (Appendix E.1) show that masking high-communicability nodes led to the most effective learning of the data structure, resulting in superior performance in downstream tasks.

Pretraining involved two complementary masking strategies: temporal masking and spatial masking (Figure 4). Spatial masking involved nullifying the timeseries data of the top k nodes with the highest communicability scores, where k is less than the total number of ROIs. Temporal masking, on the other hand, initialized all ROI signals to

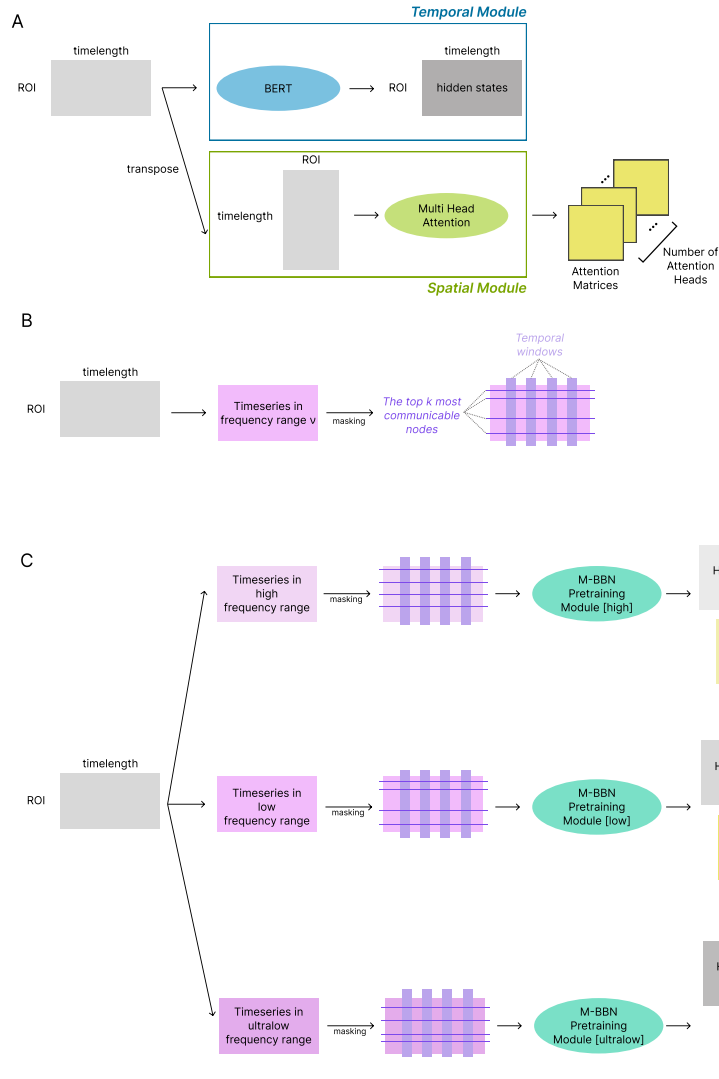


Fig. 4 MBBN Pretraining Workflow. **A.** Each frequency-divided timeseries is processed using the MBBN pretraining module, where the temporal module extracts hidden states using a BERT encoder, and the spatial module computes attention matrices via a multi-head attention mechanism. **B.** Masking strategies: spatial masking nullifies the time series data of the top k nodes with the highest communicability scores, while temporal masking zeros out ROI signals within predefined time windows. **C.** Pretraining is conducted separately for high, low, and ultralow frequency bands. Parameter sharing is applied in the temporal module but not in the spatial module. Outputs include hidden states and averaged attention matrices for each frequency range.

zero within predefined time windows. Both strategies were applied to each frequency band (ultralow, low, and high), denoted as ν .

The masking loss ($Loss_{mask}$) was calculated as the sum of L1 losses between the original BOLD signals ($BOLD_{\nu}$) and their masked counterparts ($maskedBOLD_{\nu}$):

$$Loss_{mask} = \sum_{\nu} Loss_{L1}(BOLD_{\nu}, maskedBOLD_{\nu}) \quad (10)$$

The pretraining loss was the combination of the masking loss and the spatial loss (Equation 9), which enables the model to simultaneously learn node relationships and recover masked regions. λ employed in the pretraining loss function was maintained at the same value as that used in the total loss calculation (Equation 5) during from-scratch training.

$$Loss_{pretrain} = Loss_{mask} + \lambda \cdot Loss_{spatial} \quad (11)$$

3.8.2 Temporal Masking Optimization

In temporal masking, rather than predicting a single time point, the model is tasked with predicting entire time windows. This strategy makes the task more challenging, encouraging the model to learn temporal dependencies more effectively. Masking was implemented by setting ROI signals to zero within predefined time windows.

To optimize temporal masking, we empirically tested various configurations by adjusting two parameters:

- N : the length of the masked time window.
- k : the distance between consecutive masked windows.

The best performance in downstream tasks was achieved with $N = 20$ and $k = 1$, where N ranged from 5 to 45 in multiples of 5, and k was an integer between 1 and 5.

3.8.3 Implementation Details and Dataset

Pretraining was conducted using the UK Biobank dataset, with a sequence length of 464. During finetuning, padding was applied to align shorter sequences (τ) to this fixed length, with padding added equally to both ends of the sequence $((464 - \tau)/2)$. The outputs from the pretraining process, which include hidden states and attention matrices for each frequency band, were used to initialize the MBBN model for downstream tasks. Figure 4 illustrates the pretraining workflow, including the temporal and spatial masking procedures. Temporal masking is represented by lavender rectangles, while spatial masking is depicted with purple lines.

3.9 Interpretability

MBBN computes attention matrices between Regions of Interest (ROIs) across different frequency ranges. These matrices serve as estimates of functional connectivity, making it crucial to analyze individual connections to understand their contributions to phenotype classification. This analysis offers insights into the neural mechanisms underlying the phenotype of interest.

Traditional attribution methods are not directly applicable to this model, as the relationship between attention matrices and target values is indirect. To address this challenge, we developed a novel approach inspired by GradCAM ([43]), specifically tailored to the spatial attention module described in Section 3.7.

GradCAM typically highlights important regions by computing the gradient of the loss for the target class and weighting it by the output feature maps. Similarly, we compute heatmaps by multiplying the activation values (attention matrices) with their respective gradients, as described in Equation 12. This method highlights specific functional connectivity patterns that are relevant to mental disorders. In Equation 12, f refers to the spatial attention module, $Loss_{spatial}$ corresponds to the loss term from Equation 9, k represents the frequency range (high, low, ultralow), and $input_k$ denotes the fMRI BOLD data for frequency range k ($Heatmap_k \in \mathbb{R}^{(N_{ROI} \times N_{ROI})}$).

To interpret the model’s predictions, we selected the best-performing model based on the validation dataset and applied it to the test dataset. Heatmaps were generated for true positive subjects. Analysis for false positive and false negative subjects was conducted to validate the method. For inter-group comparisons, we conducted t-tests to identify statistically significant connections ($p < 0.05$). For multiple comparison correction, we applied False Discovery Rate (FDR) (Benjamin-Hochberg method) to control for Type I errors. Then we calculated the effect size using Cohen’s d ([44]). The sign of the t-statistic indicated which group had a higher attribution score for a given connection. For example, in the classification of ADHD using the ABCD dataset, a positive t-statistic suggested that a connection contributed more significantly to the Healthy Control (HC) group than to the ADHD group.

Statistically significant connections ($p < 0.05$) and regions were analyzed, but the number of connections was too large to handle effectively. To address this, we selected only a few top connections based on the absolute values of Cohen’s d for further evaluation of their impact. An exhaustive list of all significant connections can be found in Appendix F.

$$Heatmap_k = \frac{\partial Loss_{spatial}}{\partial f_k(input_k)} \odot f_k(input_k) \quad (12)$$

3.10 Performance Comparison with Baseline Models

To evaluate the effectiveness of MBBN in learning spatiotemporal dynamics, we compared its performance with baseline models, including functional connectivity-based models (XGBoost [45], BNT [5]) and temporal dynamics models (BoLT ([6]), vanilla BERT ([39])). These models were selected based on their relevance to brain dynamics interpretation, either through static functional connectivity or sequential processing of temporal data. While functional connectivity-based models primarily rely on static representations, temporal dynamics models capture sequential patterns but do not explicitly integrate spatial relationships. MBBN addresses this gap by combining both spatiotemporal characteristics using its frequency-dividing encoder and spatial attention module. Given that MBBN is an extension of vanilla BERT with additional architectural enhancements, a direct comparison between the two provides a robust evaluation of these modifications. While MBBN demonstrated superior performance across several downstream tasks, including the ABCD ADHD classification task, with significant improvements in accuracy and AUC scores, not all tasks showed a statistically significant advantage. Detailed performance comparison is described in Appendix E.1.

To ensure a fair evaluation, we conducted statistical tests (paired t-tests) to compare the performance of MBBN with baseline models on each task. The p-values for these comparisons indicated that, although MBBN did not outperform all baseline models in every metric, the differences were not statistically significant ($p > 0.05$) in cases where baseline models showed slightly better performance. These results suggest that MBBN encodes information at a level comparable to or better than existing models while providing the additional advantage of capturing spatiotemporal dynamics, which baseline models are unable to incorporate.

4 Discussion

Discussions should be brief and focused. In some disciplines use of Discussion or ‘Conclusion’ is interchangeable. It is not mandatory to use both. Some journals prefer a section ‘Results and Discussion’ followed by a section ‘Conclusion’. Please refer to Journal-level guidance for any specific requirements. This study introduces MBBN, a novel computational framework that integrates neuroscientific principles with advanced deep learning methodologies to analyze brain dynamics. MBBN employs a scale-free, frequency-based decomposition technique that encodes distinct frequency components as individual features, effectively capturing the multi-fractal dynamics of brain activity. Additionally, the model leverages a communicability-based masking strategy during pretraining, embedding the underlying network topology into its learned representations. Through a self-attention mechanism, MBBN combines biologically informed spatial relationships with temporal context, enabling the nuanced modeling of connectivity patterns and their evolution across multiple frequency ranges. This unified framework provides a robust platform for accurate, interpretable, and personalized predictions of cognitive and clinical outcomes.

Compared to previous transformer-based models for brain imaging data (e.g., [5–8]), MBBN uniquely integrates the multi-fractal ([46–48]) and scale-free properties of neural signals ([36, 49]), essential for understanding the hierarchical and dynamic nature of brain activity ([50–52]). Unlike models relying solely on static or sequential representations ([5, 6]), or employing simplistic masking strategies ([7, 8]), MBBN’s biologically grounded approach—decomposing multifractal neural signals into interpretable frequency components and utilizing a communicability-driven masking scheme—enables it to effectively capture and reconstruct critical network hubs. By doing so, MBBN provides a more nuanced and biologically relevant representation of spatiotemporal connectivity.

Crucially, correlation analysis confirms that the connectivity derived from MBBN’s self-attention mechanism represents a novel measure, capturing information distinct from and complementary to traditional functional connectivity (FC). To elucidate this, we directly compared attention-based connectivity with FC. This revealed a strong negative correlation when analyzing raw, non-frequency-divided signals (Spearman $\rho \approx -0.6$), indicating that attention-based connectivity captures fundamentally different, complementary information rather than merely replicating static FC patterns. Of note, the correlations became considerably weaker within specific frequency bands (ranging from $\rho \approx -0.1 \sim -0.2$) (Supplementary Table C2). These findings

strongly suggest that MBBN successfully extracts unique, frequency-dependent connectivity patterns that are distinct from both traditional FC and the aggregated signal. This divergence not only validates our attention mechanism as providing a novel and meaningful measure of neural interaction but also underscores the importance of frequency-specific analysis for uncovering nuanced brain dynamics potentially missed by conventional methods. The biological plausibility of MBBN is further supported by its incorporation of the scale-free property, characterized by a power-law exponent (β), which differentiates brain states and regions based on their temporal correlation profiles ([2, 53–57]). Variations in β values are associated with functional specialization and pathological alterations ([9, 13, 14, 58]), underscoring the importance of integrating these intrinsic properties into computational models. By incorporating communicability-based masking, MBBN systematically accounts for graph-structured brain data, addressing the limitations of random masking strategies ([59, 60]) and enhancing understanding of network-level interactions ([61, 62]).

When applied to graph-structured functional brain data, random masking fails to consider node importance and the non-Euclidean nature of the data ([59, 60]), leading to uncertainties in reconstructing masked information. MBBN overcomes these limitations through a communicability-based masking strategy, which quantifies information flow across all possible network paths and emphasizes the role of high-communicability hubs in shaping network dynamics ([61, 62]). By selectively masking these critical hubs and reconstructing their activity through interactions with surrounding nodes, MBBN learns structural dependencies intrinsic to neural systems, enhancing both interpretability and robustness. This approach establishes MBBN as a foundational framework for advancing neuroimaging analysis.

MBBN demonstrated superior performance across diverse datasets, including UK Biobank, ABCD, and ABIDE, underscoring its robustness across different age groups and developmental stages. While UK Biobank includes primarily middle-aged adults, ABCD and ABIDE focus on children and adolescents during critical brain maturation periods. Unlike most functional brain transformer models ([5, 7, 8]), which are rarely validated on heterogeneous cohorts, MBBN effectively handles lifespan variability, suggesting that it captures fundamental principles of brain organization. This enables accurate predictions of clinical and cognitive outcomes across ages and provides insights into developmental trajectories and age-specific neurological markers.

Our findings revealed distinct, frequency-specific connectivity alterations distinguishing individuals with ADHD and ASD from healthy controls. In ADHD, problematic connectivity was observed in regions essential for visual and audio processing, memory formation, and attention regulation with disruptions varying significantly across frequency ranges.

In the high-frequency range, we observed significant reductions in connectivity between the Parahippocampal area 3 and multiple early visual regions, as well as between the Ventromedial visual area 2 and primary/third visual cortices. These findings imply impaired integration between visual information and memory or contextual processing systems, which may be linked to difficulties in sustaining attention, interpreting visual scenes, and integrating incoming stimuli in ADHD ([63, 64]). In the low-frequency range, decreased connectivity emerged between the Parahippocampal

area and anterior temporal, perirhinal, and orbitofrontal regions—networks typically involved in episodic memory, semantic integration, and affective regulation ([65, 66]). Additionally, weakened connections between the primary auditory cortex and multimodal association areas point to disruptions in sensory processing ([67]). These alterations suggest that ADHD may be characterized by deficits in slower, long-range communication necessary for high-level cognitive integration and stable internal state representation. Conversely, the ultralow-frequency range showed increased connectivity in ADHD, particularly between the Ventromedial visual area 3 and spatial attention regions (e.g., Lateral intraparietal area ventral, medial area 7A), as well as between emotion-related regions such as Area TF (the posterior subdivision of the Parahippocampal cortex), Area 25 (Subgenual cingulate cortex), and the anterior cingulate cortex (s32). This pattern may reflect excessive internal processing, emotional dysregulation, and inefficient attentional gating ([68]). Together, these findings indicate that ADHD involves a dynamic reconfiguration of functional brain networks across multiple timescales—with reduced integration in fast and intermediate-range communication, and hyperconnectivity in the slowest neural rhythms—potentially contributing to the core symptoms of inattention, emotional lability, and sensory processing anomalies.

Our frequency-specific analysis of the ABIDE dataset for ASD prediction revealed divergent patterns of functional connectivity alterations across spectral bands, underscoring the multi-timescale nature of network disruptions in autism spectrum disorder. In the high-frequency range, the ASD group exhibited markedly increased connectivity, particularly involving Area PGs (Posterior superior parietal lobule), Area 8 anterior ventral (within the prefrontal cortex), and Area 8Ad (Anterior dorsal prefrontal cortex) with regions implicated in executive control and higher-order social cognition (e.g., Area p32, Area 9 Middle, Dorsal Area 24d). These patterns suggest hyperconnectivity in frontoparietal and cingulo-opercular circuits, potentially reflecting compensatory or maladaptive neural synchronization related to cognitive control and social attention ([69, 70]). In the low-frequency range, increased connectivity was observed between multiple sensory and associative areas (e.g., Area PH, Primary Sensory Cortex, Auditory and ParaBelt Complexes) and Area posterior 9–46 ventral. This may reflect overintegration or inefficient filtering in low-frequency sensory-cognitive loops, contributing to the sensory hypersensitivity and perceptual integration challenges frequently reported in ASD ([71, 72]). Conversely, the ultralow-frequency range showed decreased connectivity in the ASD group compared to controls, notably in connections between Parahippocampal area 1, Area PH, and auditory complexes with Area 7PC (Precuneus) and Area Frontal Opercular 5. These connections are implicated in high-level integrative functions such as spatial awareness, self-referential processing, and multimodal integration. Reduced ultralow-frequency connectivity may reflect a breakdown in global neural coordination and internal state regulation, core deficits commonly implicated in autism ([73, 74]). Together, these findings reveal a frequency-dependent reconfiguration of functional brain networks in ASD, with fronto-executive hyperconnectivity at higher frequencies and reduced long-range integrative coupling at the slowest rhythms—highlighting potential biomarkers and targets for intervention across multiple neurophysiological timescales.

Connectivity patterns observed across frequency bands revealed a transition from local to more widespread disruptions in both ADHD and ASD. In ADHD, high-frequency alterations were primarily local, focusing on visual and memory-related circuits, while ultralow-frequency changes spanned broader fronto-parietal and cingulo-limbic networks. Similarly, ASD showed local hyperconnectivity in high and low-frequency bands, especially in frontal and sensory areas, with broader hypoconnectivity emerging only in the ultralow-frequency range. These results suggest that while both disorders exhibit frequency-specific connectivity alterations, the spatial scale of disruption expands with slower neural oscillations.

In sum, MBBN’s multifaceted and biologically informed approach to modeling spatiotemporal brain dynamics represents a significant advancement over existing transformer-based frameworks. Its comprehensive integration of neuroscientific principles, self-attention mechanisms, and frequency-specific analyses positions MBBN as a promising foundation for more accurate, interpretable, and clinically meaningful neuroscience research.

Data and Code Availability

The code is available on Github (<https://github.com/Transconnectome/MBBN>). The UKB, ABCD, and ABIDE datasets are publicly available to researchers.

Author Contributions

Sangyoon Bae conceptualized the research, implemented the core algorithms, and conducted all experiments. Junbeom Kwon contributed to code optimization and manuscript preparation.

Declarations

Nothing to declare.

Funding

This work was supported by the National Research Foundation of Korea(NRF) grant funded by the Korea government(MSIT) (No. 2021R1C1C1006503, RS-2023-00266787, RS-2023-00265406, RS-2024-00421268), by Creative-Pioneering Researchers Program through Seoul National University(No. 200-20240057), by Semi-Supervised Learning Research Grant by SAMSUNG(No.A0426-20220118), by Identify the network of brain preparation steps for concentration Research Grant by LooxidLabs(No.339-20230001), by Institute of Information & communications Technology Planning & Evaluation (IITP) grant funded by the Korea government(MSIT) [NO.RS-2021-II211343, Artificial Intelligence Graduate School Program (Seoul National University)] by the MSIT(Ministry of Science, ICT), Korea, under the Global Research Support Program in the Digital Field program(RS-2024-00421268) supervised by the IITP(Institute for Information & Communications Technology Planning & Evaluation), by the National Supercomputing Center with supercomputing resources

including technical support(KSC-2023-CRE-0568) and by the Ministry of Education of the Republic of Korea and the National Research Foundation of Korea (NRF-2021S1A3A2A02090597), and by Artificial intelligence industrial convergence cluster development project funded by the Ministry of Science and ICT(MSIT, Korea) & Gwangju Metropolitan City.

Appendix A Pretraining

A.1 Communicability

Communicability encompasses not only the shortest paths but also other types of walks between nodes p and q within a network. A network can be represented as a graph $G = (V, E)$, where V represents nodes and E represents the edges connecting the nodes. Let us denote the number of nodes as n and the number of edges as m . The adjacency matrix of the graph is $A(G) = A$, where A_{ij} takes a value of 1 if nodes i and j are connected and 0 otherwise. The communicability between nodes p and q in the network, denoted as G_{pq} , incorporates eigenvalues and eigenvectors of the adjacency matrix. Let $\lambda_1 \geq \lambda_2 \geq \dots \geq \lambda_n$ be the eigenvalues in non-increasing order, and let $\phi_j(p)$ represent the p -th element of the j -th orthonormal eigenvector corresponding to eigenvalue λ_j . Then, communicability is calculated as follows:

$$G_{pq} = \sum_{j=1}^{\infty} \phi_j(p)\phi_j(q)e^{\lambda_j} \quad (\text{A1})$$

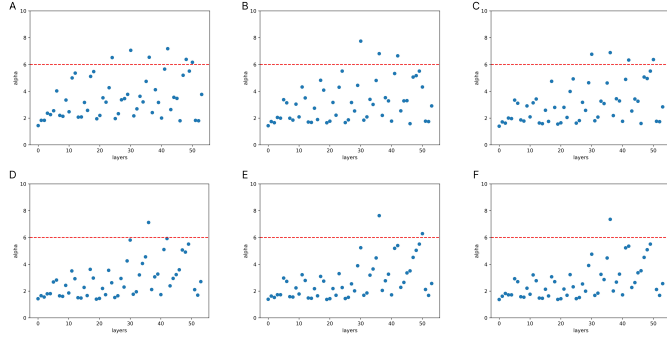
Communicability provides a measure of how efficiently information flows between nodes by considering not just direct connections but also indirect pathways weighted by their importance. This property makes communicability particularly suitable for identifying high-influence nodes in brain networks, which are then used in our pretraining masking strategy.

A.2 Effective Pretraining: Finding the Optimal Number of Epochs

Determining the optimal number of epochs for pretraining is crucial for creating an effective pretraining strategy. We utilized weightwatcher ([31]), a diagnostic tool based on traditional statistical learning theory and statistical mechanics, to identify well-trained models. Weightwatcher analyzes the norms of the weight matrix W and parameters of power-law (PL) fit on the eigenvalues of W to assess training quality without requiring data.

According to the Heavy-Tailed Self-Regularization (HT-SR) Theory, lower PL exponent (α) values indicate stronger implicit self-regularization, leading to better generalization. Consistently low α values across layers allow effective correlation flow, enabling the gradual transformation of data correlations through each layer. As shown in previous work, layers with α values below 6 are deemed well-trained, while those exceeding 6 are considered poorly trained.

In the following figures, the x-axis represents the layers, and the y-axis represents the α values. The red dotted line marks the threshold of $\alpha = 6$. The number of layers



Supplementary Figure A1 Alpha Value Changes by Pretraining Epochs (HCPMMP1 Atlas, Epochs: 100-600)

with α values above 6 converges to a single layer after epoch 500 (Supplementary Figure A1). We hypothesize that the epoch at which the pattern of layers with α values exceeding 6 stabilizes marks the optimal pretraining epoch. In our monitoring process, we utilized WeightWatcher to analyze the pretrained model at intervals of 100 epochs. We identified the critical epoch n at which the number of layer with $\alpha > 6$ converges. Subsequently, we conducted a series of fine-tuning experiments at 10-epoch intervals between epochs $n - 100$ and n to empirically determine the optimal epoch for model performance. In HCPMMP1 atlas, n was 600.

Selecting these epochs ensures that most layers in the model achieve sufficient self-regularization, improving overall generalization performance during fine-tuning.

Appendix B Interpretation of Network Properties

Measure	Modularity		Small-worldness Parameters					
	FC	Attention	γ	FC λ	σ	Attention		
						γ	λ	σ
High frequency	0.0278	0.0576	4.7683	1.4239	3.3487	9.3960	0.9220	10.1913
Low frequency	0.0251	0.0701	4.8803	1.4140	3.4514	5.6272	0.9953	5.6539
Ultralow frequency	0.0350	0.0991	4.8600	1.4794	3.2850	8.3929	0.9229	9.0941
Raw (Non-dividing)	0.0630	-0.0000	7.7804	1.6143	4.8197	5.9527	0.9254	6.4329

Supplementary Table B1 Comparison of Network Properties between FC and Attention Matrix

Our analysis of network properties provides strong evidence that frequency-specific attention matrices capture meaningful connectivity patterns that differ from traditional functional connectivity (FC).

- **Modularity** quantifies the strength of division of a network into modules or communities. It measures how well a network can be decomposed into distinct subgroups, with higher values indicating more distinct community structures where connections

within communities are denser than connections between communities. Formally, it is defined as the fraction of edges that fall within given communities minus the expected fraction if edges were distributed at random while preserving node degrees.

- **Small-worldness parameters** characterize the topological properties of a network that exhibits both high clustering and short path lengths:
 - **Gamma** (γ): The clustering coefficient ratio comparing the observed network to a random network with the same number of nodes and edges. Higher values indicate greater local connectivity and clustering, reflecting more efficient local information processing.
 - **Lambda** (λ): The characteristic path length ratio comparing the observed network to a random network. Values closer to 1 indicate efficient global integration and information transfer across the network.
 - **Sigma** (σ): The small-worldness index calculated as γ/λ . Values significantly greater than 1 indicate that the network exhibits small-world properties, characterized by high local clustering and relatively short path lengths. Small-world networks are considered optimal for information processing, combining efficient local processing with global integration.

These network metrics provide quantitative measures for assessing the topological organization of brain networks and are widely used in neuroimaging studies to characterize functional and structural connectivity patterns. Several key observations can be made from Supplementary Table B1:

1. **Frequency-dependent modularity:** The attention matrices exhibit distinct modularity and small-worldness patterns across frequency bands (high, low, and ultralow frequencies). A clear trend of increasing modularity with decreasing frequency ($0.0576 \rightarrow 0.0701 \rightarrow 0.0991$) is observed. This pattern aligns with findings from [34], which demonstrated that resting-state BOLD signals display frequency-specific network architecture, where networks that are finely subdivided in lower frequency bands become integrated into fewer networks in higher frequency bands rather than reconfigured. Such evidence supports the observation that modularity values are higher in lower frequency bands, consistent with our results.
2. **Contrasting patterns with FC:** While FC exhibits its highest modularity in the raw (unfiltered) condition (0.0630), attention-based connectivity shows essentially no modularity in the raw condition (-0.0000). This striking difference suggests that our attention mechanism captures frequency-specific network organization that is lost when analyzing the full frequency spectrum together.
3. **Small-worldness characteristics:** The small-worldness parameters (γ , λ , and σ) reveal distinct network architectures between FC and attention-based connectivity. Notably, attention matrices consistently show higher clustering (γ) and small-worldness (σ) values across frequency bands compared to FC, while maintaining more optimal path length properties (λ closer to 1). This indicates that attention-based connectivity may better preserve the small-world architecture that is characteristic of brain networks.

4. **Frequency-specific information:** Raw data without frequency decomposition fails to exhibit meaningful modularity in the attention matrix, whereas frequency-decomposed data reveals distinct modular structures. These findings suggest effective coupling between the spatial module and frequency-dividing strategy, enabling the extraction of neurobiologically relevant patterns. This observation underscores the importance of frequency-specific analysis when employing attention-based connectivity measures to characterize brain network organization.

These findings support our claim that frequency-specific attention matrices represent a valid and interpretable new form of connectivity measure, capturing network properties that complement traditional FC measures.

Appendix C Correlation Analysis Between FC and Attention-Based Connectivity

To further investigate the relationship between functional connectivity (FC) and our proposed attention-based connectivity measure, we conducted correlation analyses across different frequency bands. Spearman correlation measures the monotonic relationship between two variables by evaluating the rank order association, making it robust to outliers and nonlinear relationships. Kendall tau is a similar non-parametric measure that assesses the ordinal association between two variables by analyzing the number of concordant and discordant pairs, providing a measure of agreement in rankings. The results are presented in Table C2.

Frequency Band	Spearman Correlation	Kendall Tau
Raw (Non-dividing)	-0.6081	-0.4367
High frequency	-0.0952	-0.0700
Low frequency	-0.1459	-0.1072
Ultralow frequency	-0.1973	-0.1451

Supplementary Table C2 Correlation Analysis Between FC and Attention Matrix

The correlation analysis reveals several important insights:

1. **Complementary information:** The strong negative correlation between FC and attention-based connectivity in the raw condition (Spearman $\rho = -0.6081$, Kendall $\tau = -0.4367$) indicates that these two measures capture fundamentally different aspects of brain connectivity. This negative correlation suggests that our attention-based connectivity is not merely replicating traditional FC but providing complementary information.
2. **Frequency-specific patterns:** When examining frequency-specific bands, the correlations become considerably weaker (ranging from approximately -0.10 to -0.20), suggesting that each frequency band captures unique connectivity patterns.
3. **Methodological validity:** The consistent negative correlations across all frequency bands, albeit weaker in the frequency-specific analyses, indicate that our

attention mechanism systematically extracts connectivity information that differs from traditional FC. This suggests that attention-based connectivity represents a valid new form of connectivity measure with its interpretable meaning.

These correlation findings, combined with the network property analysis, provide strong evidence that our frequency-specific attention-based connectivity measure captures meaningful and interpretable connectivity patterns that complement traditional FC analysis. The method does not simply maximize differences between frequencies but extracts biologically relevant connectivity information specific to each frequency band.

Appendix D Ablations

D.1 The performance of the model when provided with timeseries data of a single frequency range.

Data	ABCD sex classification		UKB sex classification	
	AUROC \uparrow	Accuracy \uparrow	AUROC \uparrow	Accuracy \uparrow
Z-scored original signal	0.901 \pm 0.003	0.814 \pm 0.0031	0.942 \pm 0.014	0.876 \pm 0.006
High Frequency	0.888 \pm 0.007	0.797 \pm 0.011	0.933 \pm 0.007	0.857 \pm 0.003
Low frequency	0.884 \pm 0.005	0.784 \pm 0.011	0.936 \pm 0.004	0.850 \pm 0.015
Ultra-low Frequency	0.870 \pm 0.010	0.779 \pm 0.013	0.935 \pm 0.003	0.862 \pm 0.007
Divided Frequencies	0.916\pm0.004	0.844\pm0.006	0.975\pm0.001	0.920\pm0.001

Supplementary Table D3 Results of BERT models trained with single frequency range in the timeseries data extracted by HCP-MMP1 atlas

The core innovation of our model lies in encoding signals through frequency division and merging them within the modeling process. To identify the source of performance improvement, we conducted ablation studies focusing on single-frequency range data.

First, we examined whether frequency-divided timeseries data alone could capture the dominant signals essential for phenotype prediction. If successful, single-frequency data would outperform other inputs. However, as shown in Table D.1, single-frequency data consistently underperformed compared to the z-scored original signal. This finding suggests that the model does not rely solely on dominant signals from specific ranges but rather leverages contributions from all three frequency ranges.

Second, we analyzed the impact of merging signals from multiple frequency ranges. Results indicate that integrating signals within the model, through parameter sharing across multi-views, significantly enhances performance compared to using frequency-separated data alone. This demonstrates the importance of combining signals at the model level rather than isolating them at the data preprocessing stage.

Model	ABCD sex classification		UKB sex classification	
	AUROC \uparrow	Accuracy \uparrow	AUROC \uparrow	Accuracy \uparrow
MBBN with conv	0.825 \pm 0.009	0.726 \pm 0.009	0.947 \pm 0.003	0.870 \pm 0.002
MBBN without conv	0.916\pm0.004	0.844\pm0.006	0.975\pm0.001	0.920\pm0.001

Supplementary Table D4 Results of BERT models with a convolutional layer before BERT model

D.2 Treating fMRI signal as a sequence of discrete words.

Determining whether fMRI data should be treated as continuous variables, akin to speech, or discrete sequences, similar to natural language, is a critical design choice. Given the high sample rate of fMRI signals, we hypothesized that they resemble written sentences more closely than speech signals.

To evaluate this, we introduced convolutional layers before feeding the input into the model, inspired by speech recognition frameworks such as Wav2Vec [40]. Table D.2 reveals that treating fMRI signals as discrete word sequences yields superior performance compared to processing them as continuous variables. This result highlights the effectiveness of viewing fMRI signals as structured sequences analogous to natural language.

D.3 Frequency-dividing strategies.

Dividing Strategy	ABCD sex classification		UKB sex classification	
	AUROC \uparrow	Accuracy \uparrow	AUROC \uparrow	Accuracy \uparrow
No division	0.901 \pm 0.003	0.814 \pm 0.003	0.942 \pm 0.014	0.876 \pm 0.006
Random 2 Freq	0.903 \pm 0.004	0.818 \pm 0.004	0.969 \pm 0.003	0.911 \pm 0.003
Lorentzian-based 2 Freq	0.903 \pm 0.006	0.805 \pm 0.010	0.973 \pm 0.007	0.918 \pm 0.005
Random 3 Freq	0.900 \pm 0.006	0.803 \pm 0.008	0.972 \pm 0.002	0.918 \pm 0.003
Ours	0.916\pm0.004	0.844\pm0.006	0.975\pm0.001	0.920\pm0.001

Supplementary Table D5 Results of BERT variants trained with different frequency-dividing strategies in the timeseries data extracted by HCP-MMP1 atlas

To optimize the frequency-dividing strategy, we compared methods using Lorentzian and spline multifractal equations with alternative approaches. Results are presented in Table D.3.

First, we tested random division by selecting two random cutoff frequencies from a normal distribution. Compared to this baseline (Random 3 Freq), our method (Ours) improved AUROC by 1.11%, demonstrating the effectiveness of Lorentzian and spline multifractal equations.

Second, we evaluated division into two frequency ranges instead of three. Using Lorentzian-based boundaries (Lorentzian-based 2 Freq) led to reasonable performance but was outperformed by our three-range strategy, with a 1.44% improvement in

AUROC. This emphasizes the importance of high-frequency signals in predicting phenotypes.

In conclusion, dividing frequencies using Lorentzian and spline multifractal equations into three ranges yields superior performance, highlighting the biological significance of high-frequency components.

D.4 Spatial module and temporal module.

Module	ABCD sex classification		UKB sex classification	
	AUROC \uparrow	Accuracy \uparrow	AUROC \uparrow	Accuracy \uparrow
Spatial	0.553 \pm 0.007	0.540 \pm 0.018	0.856 \pm 0.004	0.778 \pm 0.004
Temporal	0.909 \pm 0.007	0.831 \pm 0.011	0.964 \pm 0.001	0.915 \pm 0.001
Spatiotemporal (MBBN)	0.916\pm0.004	0.844\pm0.006	0.975\pm0.001	0.921\pm0.006

Supplementary Table D6 Results of spatial and temporal modules of MBBN in the timeseries data extracted by HCP-MMP1 atlas

Table D6 illustrates the performance of individual spatial and temporal modules compared to the full MBBN spatiotemporal architecture on ABCD/UKB sex classification tasks. The results demonstrate that spatial and temporal modules interact synergistically through joint parameter updates during training. When used independently, both modules show diminished performance compared to the integrated spatiotemporal approach (MBBN). The spatial module achieves moderate performance, while the temporal module performs considerably worse on the ABCD dataset. These findings suggest that the neural dynamics captured in fMRI data require both spatial and temporal processing to maximize predictive power. The superior performance of the integrated MBBN architecture implies that allowing these modules to interact through shared loss functions and simultaneous parameter updates creates representations that better capture the complex spatiotemporal patterns in brain activity. This emphasizes the importance of modeling both spatial and temporal dimensions of neural data rather than treating them as independent components.

D.5 Number of parameters and FLOPs

Module	AUROC \uparrow	Accuracy \uparrow	FLOPs	Number of Params
Vanilla BERT (FLOPs-matched)	0.886 \pm 0.000	0.807 \pm 0.008	70,489,026,464	29,894,149
Vanilla BERT (Params-matched)	0.884 \pm 0.006	0.778 \pm 0.027	23,497,736,096	10,050,757
MBBN	0.916 \pm 0.004	0.844 \pm 0.006	70,528,086,432	11,140,695

Supplementary Table D7 Performance of vanilla BERT with parameter count or FLOPs matched to MBBN levels. Experiments were conducted on the ABCD dataset, and task was sex classification.

Table D7 demonstrates a fair comparison between MBBN and vanilla BERT models with matched computational complexity. Two variants of vanilla BERT were created: one matching MBBN’s FLOPs (70.5B vs 70.5B) and another matching MBBN’s parameter count (10.1M vs 11.1M). Despite having similar computational resources or parameter counts, MBBN significantly outperforms both Vanilla BERT variants in AUROC and accuracy. These results strongly suggest that MBBN’s superior performance cannot be attributed simply to increased model capacity or computational complexity. Rather, the architectural innovations in MBBN appear to be responsible for its enhanced effectiveness compared to vanilla BERT baselines.

Appendix E Comparison with other models

E.1 Performance comparison

Models (data form)	ABCD sex		UKB sex	
	AUROC \uparrow	Accuracy \uparrow	AUROC \uparrow	Accuracy \uparrow
XGBOOST (CC)	0.768 \pm 0.004	0.696 \pm 0.001	0.859 \pm 0.003	0.768 \pm 0.005
BNT (CC)	0.895 \pm 0.001	0.814 \pm 0.010	0.950 \pm 0.004	0.864 \pm 0.017
BolT (TD)	0.883 \pm 0.001	0.795 \pm 0.001	0.950 \pm 0.000	0.878 \pm 0.001
vanilla BERT (TD)	0.884 \pm 0.006	0.778 \pm 0.027	0.942 \pm 0.014	0.876 \pm 0.006
MBBN (TD)	0.916\pm0.004	0.844\pm0.006	0.975\pm0.001	0.921\pm0.006

Supplementary Table E8 Results of models trained from scratch predicting biological phenotypes. Atlas is HCP MMP 1. CC denotes correlation-based connectivity and TD denotes temporal dynamics.

Models	ABCD sex		UKB sex	
	AUROC \uparrow	Accuracy \uparrow	AUROC \uparrow	Accuracy \uparrow
XGBOOST (CC)	0.812 \pm 0.004	0.734 \pm 0.003	0.905 \pm 0.004	0.884 \pm 0.002
BNT (CC)	0.920 \pm 0.006	0.839 \pm 0.012	0.982 \pm 0.001	0.934 \pm 0.092
BolT (TD)	0.911 \pm 0.002	0.826 \pm 0.003	0.982 \pm 0.000	0.932 \pm 0.001
vanilla BERT (TD)	0.901 \pm 0.007	0.818 \pm 0.017	0.980 \pm 0.001	0.925 \pm 0.005
MBBN (TD)	0.918\pm0.002	0.831\pm0.009	0.987\pm0.001	0.934\pm0.008

Supplementary Table E9 Results of models trained from scratch predicting biological phenotypes. Atlas is Schaefer 400, 17 Networks. CC denotes correlation-based connectivity and TD denotes temporal dynamics.

The tables above (Supplementary Table E8, E9, E10, E11, E12, E13) present a comparison of various models, atlases, and metrics for different downstream tasks trained from scratch. In these tables, (CC) refers to correlation-based connectivity, and (TD) represents temporal dynamics. Specifically, (CC) denotes Pearson correlation

Models (data form)	UKB depression		ABCD depression	
	MAE ↓	MSE ↓	AUROC ↑	Accuracy ↑
XGBOOST (CC)	2.417±0.025	12.342±0.151	0.548±0.026	0.829±0.000
BNT (CC)	2.276±0.015	13.989±0.682	0.536±0.008	0.849±0.003
BolT (TD)	2.217±0.022	12.729±0.290	0.541±0.016	0.843±0.003
vanilla BERT (TD)	2.194±0.039	12.751±0.780	0.5147±0.014	0.847±0.003
MBBN (TD)	2.210 ±0.041	13.205±0.956	0.556±0.025	0.718±0.028

Supplementary Table E10 Results of models trained from scratch predicting clinical outcomes, atlas is HCP-MMP1. CC denotes correlation-based connectivity and TD denotes temporal dynamics.

Models (data form)	UKB depression		ABCD depression	
	MAE ↓	MSE ↓	AUROC ↑	Accuracy ↑
XGBOOST (CC)	2.408±0.002	11.942±0.052	0.581±0.012	0.833±0.003
BNT (CC)	2.329±0.012	15.179±2.730	0.579±0.018	0.842±0.010
BolT (TD)	2.201±0.004	13.044±0.301	0.585±0.011	0.844±0.005
vanilla BERT (TD)	2.230±0.006	13.359±0.479	0.586±0.040	0.846±0.004
MBBN (TD)	2.249 ±0.005	14.486±0.282	0.641±0.018	0.777±0.013

Supplementary Table E11 Results of models trained from scratch predicting clinical outcomes, atlas is Schaefer 400, 17 Networks. CC denotes correlation-based connectivity, and TD denotes temporal dynamics.

Models (data form)	UKB fluid intelligence		ABCD fluid intelligence	
	MAE ↓	MSE ↓	MAE ↓	MSE ↓
XGBOOST (CC)	1.609±0.009	4.078±0.086	0.787±0.002	0.987±0.033
BNT (CC)	1.581±0.023	3.993±0.516	0.793±0.008	1.061±0.093
BolT (TD)	1.589±0.002	3.973±0.006	0.728±0.004	0.845±0.010
vanilla BERT (TD)	1.597±0.015	4.081±0.094	0.722±0.005	0.838±0.036
MBBN (TD)	1.630 ±0.006	4.225±0.125	0.717±0.012	0.825±0.034

Supplementary Table E12 Results of models trained from scratch predicting cognitive outcomes, atlas is HCPMMP1. CC denotes correlation-based connectivity and TD denotes temporal dynamics.

computed on temporal dynamics. Across most tasks, MBBN (highlighted in color) generally outperforms or shows comparable performance to other baseline models.

For instance, in the ABCD depression classification task, the dataset’s imbalance in the depression-HC ratio naturally leads to high regular accuracy. However, MBBN demonstrates robustness against this imbalance by achieving more balanced performance metrics compared to other models (Table E10, E11).

Tables E14 and E15 present a comparison across models and metrics for various fine-tuning tasks. Here, MBBN is compared under different pretraining strategies:

- MBBN [from scratch]: Trained without pretraining.

Models (data form)	UKB fluid intelligence		ABCD fluid intelligence	
	MAE ↓	MSE ↓	MAE ↓	MSE ↓
XGBOOST (CC)	1.600±0.002	4.003±0.025	0.779±0.008	0.970±0.011
BNT (CC)	1.552±0.019	4.459±2.127	0.781±0.020	0.845±0.086
BolT (TD)	1.576±0.006	3.919±0.013	0.718±0.005	0.822±0.016
vanilla BERT (TD)	1.585±0.020	3.985±0.105	0.721±0.018	0.823±0.039
MBBN (TD)	1.628±0.051	4.205±0.282	0.719±0.013	0.828±0.028

Supplementary Table E13 Results of models trained from scratch predicting cognitive outcomes, atlas is Schaefer 400, 17 Networks. CC denotes correlation-based connectivity, and TD denotes temporal dynamics.

Models (data form)	ABCD ADHD classification		ABIDE ASD classification	
	AUROC ↑	Accuracy ↑	AUROC ↑	Accuracy ↑
XGBOOST (CC)	0.598±0.010	0.570±0.005	0.531±0.020	0.487±0.006
BNT (CC)	0.634±0.008	0.606±0.014	0.575±0.013	0.567±0.019
BolT (TD)	0.603±0.005	0.592±0.010	0.650±0.064	0.598±0.057
Vanilla BERT (TD)	0.609±0.020	0.592±0.015	0.583±0.004	0.542±0.021
MBBN [from scratch] (TD)	0.598±0.009	0.589±0.024	0.654±0.134	0.521±0.059
MBBN [random] (TD)	0.603±0.032	0.589±0.026	0.601±0.180	0.534±0.082
MBBN [low] (TD)	0.615±0.009	0.602±0.011	0.583±0.084	0.547±0.098
MBBN [high] (TD)	0.628±0.001	0.609±0.011	0.672±0.079	0.646±0.078

Supplementary Table E14 Finetuning results of pre-trained BERT models with different pretraining loss (HCP-MMP1 atlas). CC denotes correlation-based connectivity, TD denotes temporal dynamics, and MBBN represents our proposed model. The [random], [low], and [high] variants indicate different pretraining strategies based on masking node communicability.

Models (data form)	ABCD ADHD classification		ABIDE ASD classification	
	AUROC ↑	Accuracy ↑	AUROC ↑	Accuracy ↑
XGBOOST (CC)	0.594±0.008	0.564±0.006	0.660±0.023	0.629±0.030
BNT (CC)	0.620±0.018	0.599±0.018	0.715±0.045	0.652±0.077
BolT (TD)	0.599±0.010	0.589±0.011	0.608±0.028	0.578±0.027
Vanilla BERT (TD)	0.604±0.017	0.600±0.008	0.664±0.148	0.667±0.059
MBBN [from scratch] (TD)	0.614±0.020	0.610±0.011	0.800±0.067	0.563±0.051
MBBN [random] (TD)	0.596±0.014	0.593±0.032	0.696±0.052	0.563±0.088
MBBN [low] (TD)	0.584±0.033	0.574±0.034	0.500±0.051	0.479±0.059
MBBN [high] (TD)	0.618±0.019	0.580±0.035	0.822±0.019	0.563±0.051

Supplementary Table E15 Finetuning results of pre-trained BERT models with different pretraining loss (Schaefer 400 atlas). CC denotes correlation-based connectivity, TD denotes temporal dynamics, and MBBN represents our proposed model. The [random], [low], and [high] variants indicate different pretraining strategies based on masking node communicability.

- MBBN [low]: Pretrained with masking loss that targets nodes with low communicability.

- MBBN [random]: Pretrained with random masking loss.
- MBBN [high]: Pretrained with masking loss that targets nodes with high communicability.

MBBN [high], highlighted in color, consistently outperforms or matches the performance of other baseline models and pretraining strategies across various tasks. This result emphasizes the effectiveness of the high-communicability masking strategy in enhancing model generalization and fine-tuning performance.

E.2 FLOPs and number of parameters

The parameter count difference between our proposed MBBN model and the baseline models (Table E16) stems from our architectural design, which processes data through three separate streams. This design choice was intentional to capture complex patterns through specialized processing pathways. While this results in a higher parameter count, our ablation studies (Appendix D.5) demonstrate that the performance improvements arise primarily from the model’s architecture rather than simply from increased capacity.

Models (data form)	Number of parameters	FLOPs
XGBOOST (CC)	6100	400
BNT (CC)	3,787,250	1,805,681,216
BolT (TD)	9,597,062	4,226,217,120
Vanilla BERT (TD)	10,050,757	23,497,736,096
MBBN (TD)	11,140,695	70,528,086,432

Supplementary Table E16 The table shows the number of parameters and FLOPs of baseline models used in this study and MBBN (our model).

Appendix F Interpretability

In the following tables, two regions involved in connectivity (based on HCP-MMP1) are presented, along with whether the connectivity shows higher scores in the disorder group or the healthy control (HC) group. Additionally, corrected p-values and Cohen’s d scores were rounded to three decimal places. Due to space limitations, only the top 100 connectivity pairs are displayed.

Supplementary Table F17: Top connectivity features in high-frequency range of ABCD ADHD prediction.

Region 1	Region 2	Corrected p-value	Disorder/HC	Cohen's d
Fourth Visual Area	ParaHippocampal Area 3	< 0.001	HC	0.654
Second Visual Area	ParaHippocampal Area 3	< 0.001	HC	0.645
Polar 10p	ProStriate Area	< 0.001	HC	0.643
Primary Visual Cortex	VentroMedial Visual Area 2	< 0.001	HC	0.638
Area PFt	ParaHippocampal Area 3	< 0.001	HC	0.636
Third Visual Area	VentroMedial Visual Area 2	< 0.001	HC	0.636
Second Visual Area	VentroMedial Visual Area 2	< 0.001	HC	0.633
Second Visual Area	ProStriate Area	< 0.001	HC	0.633
Area Lateral Occipital 2	VentroMedial Visual Area 2	< 0.001	HC	0.627
Third Visual Area	VentroMedial Visual Area 1	< 0.001	HC	0.627
Area 11l	ProStriate Area	< 0.001	HC	0.626
Third Visual Area	ParaHippocampal Area 3	< 0.001	HC	0.623
Primary Visual Cortex	ParaHippocampal Area 3	< 0.001	HC	0.618
Posterior OFC Complex	Frontal Opercular Area 3	< 0.001	HC	0.616
Area 2	ParaHippocampal Area 3	< 0.001	HC	0.613
Posterior OFC Complex	Anterior Agranular Insula Complex	< 0.001	HC	0.612
Third Visual Area	ProStriate Area	< 0.001	HC	0.611
Fourth Visual Area	VentroMedial Visual Area 2	< 0.001	HC	0.61
Area posterior 10p	Frontal Opercular Area 4	< 0.001	HC	0.606
Area 47m	Frontal Opercular Area 4	< 0.001	HC	0.606
Posterior OFC Complex	Frontal Opercular Area 4	< 0.001	HC	0.604
Anterior IntraParietal Area	VentroMedial Visual Area 1	< 0.001	HC	0.601
Area 47l (47 lateral)	Frontal Opercular Area 4	< 0.001	HC	0.597
Area 10r	Frontal Opercular Area 4	< 0.001	HC	0.596

Continued on next page

Supplementary Table F17 – continued from previous page

Region 1	Region 2	Corrected p-value	Disorder/HC	Cohen's d
Area 10r	Frontal Opercular Area 3	< 0.001	HC	0.589
Area 11l	Dorsal Transitional Visual Area	< 0.001	HC	0.589
Primary Visual Cortex	VentroMedial Visual Area 1	< 0.001	HC	0.589
Area TemporoParietoOccipital Junction 1	ProStriate Area	< 0.001	HC	0.587
Second Visual Area	VentroMedial Visual Area 1	< 0.001	HC	0.587
Orbital Frontal Complex	Frontal Opercular Area 4	< 0.001	HC	0.587
Area 13l	Anterior Agranular Insula Complex	< 0.001	HC	0.587
Fourth Visual Area	VentroMedial Visual Area 1	< 0.001	HC	0.584
Posterior InferoTemporal complex	VentroMedial Visual Area 2	< 0.001	HC	0.582
Orbital Frontal Complex	Anterior Agranular Insula Complex	< 0.001	HC	0.581
Polar 10p	Area 23c	< 0.001	HC	0.578
Polar 10p	VentroMedial Visual Area 1	< 0.001	HC	0.578
Fourth Visual Area	Frontal Opercular Area 3	< 0.001	HC	0.577
Area 31pd	VentroMedial Visual Area 1	< 0.001	HC	0.575
Area Lateral Occipital 1	ProStriate Area	< 0.001	HC	0.575
Insular Granular Complex	ProStriate Area	< 0.001	HC	0.574
Primary Auditory Cortex	ProStriate Area	< 0.001	HC	0.574
Area 5L	ParaHippocampal Area 3	< 0.001	HC	0.572
Area 47m	ProStriate Area	< 0.001	HC	0.571
Anterior IntraParietal Area	ParaHippocampal Area 3	< 0.001	HC	0.57
Area Lateral Occipital 1	ParaHippocampal Area 3	< 0.001	HC	0.569
Area V4t	ParaHippocampal Area 3	< 0.001	HC	0.568
Area dorsal 23 a+b	ParaHippocampal Area 3	< 0.001	HC	0.567
Area 10v	Frontal Opercular Area 4	< 0.001	HC	0.567
Area V3B	Anterior Ventral Insular Area	< 0.001	HC	0.565

Continued on next page

Supplementary Table F17 – continued from previous page

Region 1	Region 2	Corrected p-value	Disorder/HC	Cohen's d
Posterior InferoTemporal complex	ParaHippocampal Area 3	< 0.001	HC	0.564
Area 31pd	ParaHippocampal Area 3	< 0.001	HC	0.563
Area V3CD	ProStriate Area	< 0.001	HC	0.562
Area V3B	Anterior Agranular Insula Complex	< 0.001	HC	0.562
Area V3CD	PeriSylvian Language Area	< 0.001	HC	0.562
Middle Temporal Area	VentroMedial Visual Area 1	< 0.001	HC	0.561
Medial Belt Complex	ProStriate Area	< 0.001	HC	0.561
Fourth Visual Area	ProStriate Area	< 0.001	HC	0.561
Area TemporoParietoOccipital Junction 2	VentroMedial Visual Area 1	< 0.001	HC	0.56
VentroMedial Visual Area 1	VentroMedial Visual Area 2	< 0.001	HC	0.559
Polar 10p	Area V3B	< 0.001	HC	0.559
Area 52	ProStriate Area	< 0.001	HC	0.559
Third Visual Area	Ventral Visual Complex	< 0.001	HC	0.557
Area Lateral Occipital 1	PeriSylvian Language Area	< 0.001	HC	0.556
Area 47l (47 lateral)	ProStriate Area	< 0.001	HC	0.556
Area 10v	Frontal Opercular Area 3	< 0.001	HC	0.555
Area 10v	Area 23c	< 0.001	HC	0.554
Fourth Visual Area	PeriSylvian Language Area	< 0.001	HC	0.553
Area 11l	Sixth Visual Area	< 0.001	HC	0.553
Area OP4-PV	ParaHippocampal Area 3	< 0.001	HC	0.553
Third Visual Area	PeriSylvian Language Area	< 0.001	HC	0.552
Lateral Area 7A	ParaHippocampal Area 3	< 0.001	HC	0.552
Area 10r	Middle Insular Area	< 0.001	HC	0.551
Medial Area 7P	ProStriate Area	< 0.001	HC	0.55
Area PGs	VentroMedial Visual Area 1	< 0.001	HC	0.55

Continued on next page

Supplementary Table F17 – continued from previous page

Region 1	Region 2	Corrected p-value	Disorder/HC	Cohen's d
Area Lateral IntraParietal dorsal	Primary Visual Cortex	< 0.001	HC	0.55
Area 47l (47 lateral)	Anterior Ventral Insular Area	< 0.001	HC	0.549
Area TF	Area TF	< 0.001	HC	0.549
Medial Area 7P	ParaHippocampal Area 3	< 0.001	HC	0.549
Primary Visual Cortex	ProStriate Area	< 0.001	HC	0.549
PreCuneus Visual Area	VentroMedial Visual Area 1	< 0.001	HC	0.549
Area 7PC	ParaHippocampal Area 3	< 0.001	HC	0.549
Area Lateral Occipital 1	Anterior Ventral Insular Area	< 0.001	HC	0.548
Area IntraParietal 0	ParaHippocampal Area 3	< 0.001	HC	0.548
Area Lateral Occipital 2	ParaHippocampal Area 3	< 0.001	HC	0.547
Area TE1 posterior	Dorsal Transitional Visual Area	< 0.001	HC	0.547
Area PGs	ProStriate Area	< 0.001	HC	0.545
Area 31a	ParaHippocampal Area 3	< 0.001	HC	0.545
Area 10v	VentroMedial Visual Area 1	< 0.001	HC	0.545
Area 23d	ParaHippocampal Area 3	< 0.001	HC	0.545
Area FST	ParaHippocampal Area 3	< 0.001	HC	0.545
Area TemporoParietoOccipital Junction 3	VentroMedial Visual Area 1	< 0.001	HC	0.543
Area 13l	Frontal Opercular Area 4	< 0.001	HC	0.543
Area Lateral Occipital 1	VentroMedial Visual Area 1	< 0.001	HC	0.543
VentroMedial Visual Area 1	VentroMedial Visual Area 1	< 0.001	HC	0.542
Area V3CD	Anterior Ventral Insular Area	< 0.001	HC	0.542
Area V3CD	ParaHippocampal Area 3	< 0.001	HC	0.542
Area Frontal Opercular 5	ProStriate Area	< 0.001	HC	0.541
Area 31p ventral	ParaHippocampal Area 3	< 0.001	HC	0.541
Area Lateral Occipital 3	Frontal Opercular Area 3	< 0.001	HC	0.541

Continued on next page

Supplementary Table F17 – continued from previous page

Region 1	Region 2	Corrected p-value	Disorder/HC	Cohen's d
Polar 10p	Dorsal Transitional Visual Area	< 0.001	HC	0.541

Supplementary Table F18: Top connectivity features in low frequency range of ABCD ADHD prediction

Region 1	Region 2	Corrected p-value	Disorder/HC	Cohen's d
Area TG dorsal	Area PH	< 0.001	HC	0.684
Area TE1 anterior	Area PH	< 0.001	HC	0.669
Area anterior 47r	Area PH	< 0.001	HC	0.661
Area TG Ventral	Area PH	< 0.001	HC	0.65
Primary Auditory Cortex	Area	< 0.001	HC	0.646
Perirhinal Ectorhinal Cortex	Area PH	< 0.001	HC	0.628
Primary Auditory Cortex	Area V3CD	< 0.001	HC	0.625
Area TE2 anterior	Area PH	< 0.001	HC	0.62
Orbital Frontal Complex	Area PH	< 0.001	HC	0.614
Primary Auditory Cortex	Area anterior 10p	< 0.001	HC	0.61
Primary Auditory Cortex	Area PH	< 0.001	HC	0.602
Area TG dorsal	Area V4t	< 0.001	HC	0.602
Dorsal Area 24d	Area PH	< 0.001	HC	0.601
Area 10d	Area PH	< 0.001	HC	0.594
ParaHippocampal Area 3	Area PH	< 0.001	HC	0.593
Area anterior 47r	Area V4t	< 0.001	HC	0.592
Area	Area PH	< 0.001	HC	0.585
ProStriate Area	Area anterior 47r	< 0.001	HC	0.585
Area TE2 posterior	Area V4t	< 0.001	HC	0.585
Area TG dorsal	Area	< 0.001	HC	0.579
Area V4t	Area PH	< 0.001	HC	0.579
Area 45	Area	< 0.001	HC	0.577
Area 47m	Area	< 0.001	HC	0.577
Frontal Opercular Area 2	Area	< 0.001	HC	0.576

Continued on next page

Supplementary Table F18 – continued from previous page

Region 1	Region 2	Corrected p-value	Disorder/HC	Cohen's d
Primary Auditory Cortex	Area anterior 47r	< 0.001	HC	0.575
Area TG Ventral	Area V4t	< 0.001	HC	0.568
Polar 10p	Area PH	< 0.001	HC	0.566
ProStriate Area	Area V4t	< 0.001	HC	0.564
Area 47s	Area PH	< 0.001	HC	0.564
Area TG dorsal	Fusiform Face Complex	< 0.001	HC	0.563
Area anterior 47r	Area	< 0.001	HC	0.558
Area STGa	Area PH	< 0.001	HC	0.558
Area 10v	Area PH	< 0.001	HC	0.557
Primary Auditory Cortex	Area	< 0.001	HC	0.557
Frontal Opercular Area 3	Area	< 0.001	HC	0.553
Area OP1-SII	Area anterior 47r	< 0.001	HC	0.552
Area TemporoParietoOccipital Junction 1	Area anterior 47r	< 0.001	HC	0.552
Superior Temporal Visual Area	Area anterior 47r	< 0.001	HC	0.552
Area TE2 posterior	Area PH	< 0.001	HC	0.55
ProStriate Area	Area	< 0.001	HC	0.547
Fusiform Face Complex	Area anterior 47r	< 0.001	HC	0.542
Area STGa	Area	< 0.001	HC	0.541
Area posterior 47r	Area PH	< 0.001	HC	0.54
Area 25	Area PH	< 0.001	HC	0.54
Auditory 4 Complex	Area V3CD	< 0.001	HC	0.539
Area 10d	Area V4t	< 0.001	HC	0.539
Primary Auditory Cortex	Area V4t	< 0.001	HC	0.538
Area anterior 47r	Area anterior 47r	< 0.001	HC	0.538
ParaHippocampal Area 3	Area anterior 47r	< 0.001	HC	0.536

Continued on next page

Supplementary Table F18 – continued from previous page

Region 1	Region 2	Corrected p-value	Disorder/HC	Cohen's d
Dorsal area 6	Area PH	< 0.001	HC	0.535
Area anterior 10p	Area V4t	< 0.001	HC	0.535
Area 47m	Area PH	< 0.001	HC	0.535
Area 8B	Area PH	< 0.001	HC	0.535
Primary Visual Cortex	Area PH	< 0.001	HC	0.534
Area STSv anterior	Area PH	< 0.001	HC	0.534
Area TF	Area PH	< 0.001	HC	0.534
Area V6A	Area PH	< 0.001	HC	0.533
Area TG dorsal	Area V3CD	< 0.001	HC	0.533
Middle Temporal Area	Area PH	< 0.001	HC	0.533
Area OP2-3-VS	Area anterior 47r	< 0.001	HC	0.533
Area 47s	Area	< 0.001	HC	0.533
Posterior OFC Complex	Area PH	< 0.001	HC	0.532
Perirhinal Ectorhinal Cortex	Area V4t	< 0.001	HC	0.532
Area 10v	Area	< 0.001	HC	0.532
Area posterior 10p	Area PH	< 0.001	HC	0.531
Area anterior 10p	Area PH	< 0.001	HC	0.531
Area 47l (47 lateral)	Area PH	< 0.001	HC	0.53
Area 9 Middle	Area PH	< 0.001	HC	0.53
Area STSd posterior	Area PH	< 0.001	HC	0.53
Area TE2 posterior	Area anterior 47r	< 0.001	HC	0.529
Area TE1 anterior	Area V4t	< 0.001	HC	0.529
Area PHT	Area PH	< 0.001	HC	0.528
Area PFt	Area anterior 47r	< 0.001	HC	0.527
Area TE1 Middle	Area PH	< 0.001	HC	0.526
Area STSd anterior	Area PH	< 0.001	HC	0.526

Continued on next page

Supplementary Table F18 – continued from previous page

Region 1	Region 2	Corrected p-value	Disorder/HC	Cohen's d
Area 47s	Area	< 0.001	HC	0.525
RetroSplenial Complex	Area PH	< 0.001	HC	0.525
ParaHippocampal Area 1	Area PH	< 0.001	HC	0.525
Entorhinal Cortex	Area PH	< 0.001	HC	0.524
Supplementary and Cingulate Eye Field	Area	< 0.001	HC	0.524
Area PGp	Area PH	< 0.001	HC	0.524
Area TG dorsal	Area	< 0.001	HC	0.524
Dorsal area 6	Area	< 0.001	HC	0.524
Area anterior 47r	Fourth Visual Area	< 0.001	HC	0.523
Area PFcm	Area PH	< 0.001	HC	0.523
Supplementary and Cingulate Eye Field	Area V3CD	< 0.001	HC	0.523
Area 10r	Area PH	< 0.001	HC	0.522
Area	Area PH	< 0.001	HC	0.521
Eighth Visual Area	Area	< 0.001	HC	0.521
Area TE2 posterior	Area	< 0.001	HC	0.52
VentroMedial Visual Area 1	Polar 10p	< 0.001	HC	0.519
Ventral Visual Complex	Area TG Ventral	< 0.001	HC	0.519
Area 31p ventral	Area PH	< 0.001	HC	0.519
Fourth Visual Area	Area PH	< 0.001	HC	0.519
ParaHippocampal Area 3	Fourth Visual Area	< 0.001	HC	0.518
Area 7m	Area PH	< 0.001	HC	0.518
Area p32	Area PH	< 0.001	HC	0.517
Auditory 4 Complex	Area	< 0.001	HC	0.517
Area FST	Area PH	< 0.001	HC	0.517

Continued on next page

Supplementary Table F18 – continued from previous page

Region 1	Region 2	Corrected p-value	Disorder/HC	Cohen's d
Area anterior 9-46v	Area PH	< 0.001	HC	0.516

Supplementary Table F19: Top connectivity features in ultralow frequency range of ABCD ADHD prediction

Region 1	Region 2	Corrected p-value	Disorder/HC	Cohen's d
Area Lateral IntraParietal ventral	VentroMedial Visual Area 3	< 0.001	ADHD	1.109
Area s32	ParaHippocampal Area 3	< 0.001	ADHD	1.062
Area TF	Area 25	< 0.001	ADHD	1.028
Inferior 6-8 Transitional Area	VentroMedial Visual Area 3	< 0.001	ADHD	1.016
Area TF	Area s32	< 0.001	ADHD	1.007
Ventral Visual Complex	Area V3B	< 0.001	ADHD	1.002
Area TA2	VentroMedial Visual Area 3	< 0.001	ADHD	1.002
Medial Area 7A	VentroMedial Visual Area 3	< 0.001	ADHD	1.0
Area 25	Area TF	< 0.001	ADHD	0.994
Area IntraParietal 0	VentroMedial Visual Area 3	< 0.001	ADHD	0.994
Area 25	ParaHippocampal Area 3	< 0.001	ADHD	0.993
Premotor Eye Field	VentroMedial Visual Area 3	< 0.001	ADHD	0.99
Area TF	Orbital Frontal Complex	< 0.001	ADHD	0.99
Frontal Eye Fields	VentroMedial Visual Area 3	< 0.001	ADHD	0.979
Area 13l	Area TF	< 0.001	ADHD	0.975
Area Lateral IntraParietal ventral	Ventral Visual Complex	< 0.001	ADHD	0.969
Ventral Area 6	VentroMedial Visual Area 3	< 0.001	ADHD	0.968
Frontal Eye Fields	Eighth Visual Area	< 0.001	ADHD	0.968
Area 10r	Area TF	< 0.001	ADHD	0.963
Medial Area 7A	Eighth Visual Area	< 0.001	ADHD	0.96
Lateral Area 7P	VentroMedial Visual Area 3	< 0.001	ADHD	0.959
Inferior 6-8 Transitional Area	Ventral Visual Complex	< 0.001	ADHD	0.955
Premotor Eye Field	Ventral Visual Complex	< 0.001	ADHD	0.955
Area posterior 9-46v	VentroMedial Visual Area 3	< 0.001	ADHD	0.955

Continued on next page

Supplementary Table F19 – continued from previous page

Region 1	Region 2	Corrected p-value	Disorder/HC	Cohen's d
Medial IntraParietal Area	VentroMedial Visual Area 3	< 0.001	ADHD	0.954
Area 10r	ParaHippocampal Area 3	< 0.001	ADHD	0.953
Orbital Frontal Complex	Area TF	< 0.001	ADHD	0.948
Frontal Eye Fields	Posterior InferoTemporal complex	< 0.001	ADHD	0.948
Ventral IntraParietal Complex	VentroMedial Visual Area 3	< 0.001	ADHD	0.945
Area a24	Area TF	< 0.001	ADHD	0.944
Area IFSp	VentroMedial Visual Area 3	< 0.001	ADHD	0.939
Area 6 anterior	VentroMedial Visual Area 3	< 0.001	ADHD	0.938
Frontal Eye Fields	Ventral Visual Complex	< 0.001	ADHD	0.934
Area 8BM	Area TF	< 0.001	ADHD	0.934
Area IntraParietal 1	Area TF	< 0.001	ADHD	0.934
Area s32	Area TF	< 0.001	ADHD	0.934
Posterior InferoTemporal complex	Orbital Frontal Complex	< 0.001	ADHD	0.933
Area V3B	VentroMedial Visual Area 3	< 0.001	ADHD	0.932
IntraParietal Sulcus Area 1	VentroMedial Visual Area 3	< 0.001	ADHD	0.932
Area TF	Area V3B	< 0.001	ADHD	0.932
Area IFJa	Posterior InferoTemporal complex	< 0.001	ADHD	0.93
IntraParietal Sulcus Area 1	Ventral Visual Complex	< 0.001	ADHD	0.927
Area a24	ParaHippocampal Area 3	< 0.001	ADHD	0.927
Area 6 anterior	Ventral Visual Complex	< 0.001	ADHD	0.926
Area 46	Eighth Visual Area	< 0.001	ADHD	0.925
Area Lateral IntraParietal ventral	Fourth Visual Area	< 0.001	ADHD	0.923
Inferior 6-8 Transitional Area	ParaHippocampal Area 3	< 0.001	ADHD	0.923
Area IFJp	VentroMedial Visual Area 3	< 0.001	ADHD	0.921
Lateral Area 7P	Ventral Visual Complex	< 0.001	ADHD	0.92
Inferior 6-8 Transitional Area	VentroMedial Visual Area 2	< 0.001	ADHD	0.92

Continued on next page

Supplementary Table F19 – continued from previous page

Region 1	Region 2	Corrected p-value	Disorder/HC	Cohen's d
Area dorsal 32	Area TF	< 0.001	ADHD	0.92
Area TF	Area a24	< 0.001	ADHD	0.919
Area IntraParietal 1	VentroMedial Visual Area 3	< 0.001	ADHD	0.918
Posterior OFC Complex	Area TF	< 0.001	ADHD	0.917
Inferior 6-8 Transitional Area	Eighth Visual Area	< 0.001	ADHD	0.917
Area 10r	Posterior InferoTemporal complex	< 0.001	ADHD	0.916
Area IFSp	Posterior InferoTemporal complex	< 0.001	ADHD	0.916
Area 6 anterior	Area Lateral Occipital 2	< 0.001	ADHD	0.916
Anterior 24 prime	VentroMedial Visual Area 3	< 0.001	ADHD	0.913
Area IFJa	Area TF	< 0.001	ADHD	0.912
Area s32	Posterior InferoTemporal complex	< 0.001	ADHD	0.911
Area IntraParietal 0	ParaHippocampal Area 3	< 0.001	ADHD	0.91
Area 55b	VentroMedial Visual Area 3	< 0.001	ADHD	0.907
Inferior 6-8 Transitional Area	Fourth Visual Area	< 0.001	ADHD	0.907
Anterior Ventral Insular Area	Posterior InferoTemporal complex	< 0.001	ADHD	0.906
Area Lateral IntraParietal ventral	Eighth Visual Area	< 0.001	ADHD	0.906
Area p32 prime	VentroMedial Visual Area 3	< 0.001	ADHD	0.905
Medial IntraParietal Area	Ventral Visual Complex	< 0.001	ADHD	0.904
Area Lateral IntraParietal ventral	VentroMedial Visual Area 1	< 0.001	ADHD	0.904
Area p32	Area TF	< 0.001	ADHD	0.903
Area TA2	Eighth Visual Area	< 0.001	ADHD	0.902
Area 8Ad	Area TF	< 0.001	ADHD	0.902
Area Lateral IntraParietal ventral	VentroMedial Visual Area 2	< 0.001	ADHD	0.902
Area 6 anterior	Eighth Visual Area	< 0.001	ADHD	0.901
Premotor Eye Field	Eighth Visual Area	< 0.001	ADHD	0.899
Area STSv anterior	Area TF	< 0.001	ADHD	0.899

Continued on next page

Supplementary Table F19 – continued from previous page

Region 1	Region 2	Corrected p-value	Disorder/HC	Cohen's d
Medial Area 7A	Ventral Visual Complex	< 0.001	ADHD	0.897
Posterior OFC Complex	Posterior InferoTemporal complex	< 0.001	ADHD	0.896
Area 55b	Posterior InferoTemporal complex	< 0.001	ADHD	0.895
Area 25	Posterior InferoTemporal complex	< 0.001	ADHD	0.894
Area PF Opercular	VentroMedial Visual Area 3	< 0.001	ADHD	0.893
Area IFJp	VentroMedial Visual Area 1	< 0.001	ADHD	0.891
Ventral IntraParietal Complex	Ventral Visual Complex	< 0.001	ADHD	0.891
Anterior Agranular Insula Complex	VentroMedial Visual Area 3	< 0.001	ADHD	0.891
Area 55b	Ventral Visual Complex	< 0.001	ADHD	0.89
Entorhinal Cortex	ParaHippocampal Area 3	< 0.001	ADHD	0.889
Area 46	VentroMedial Visual Area 3	< 0.001	ADHD	0.889
Area STSd anterior	Area TF	< 0.001	ADHD	0.887
Area TF	Area IntraParietal 2	< 0.001	ADHD	0.887
Area 6 anterior	ParaHippocampal Area 3	< 0.001	ADHD	0.887
Area IFJp	Posterior InferoTemporal complex	< 0.001	ADHD	0.886
Frontal Opercular Area 4	VentroMedial Visual Area 3	< 0.001	ADHD	0.886
Area IFSp	Ventral Visual Complex	< 0.001	ADHD	0.884
Middle Insular Area	VentroMedial Visual Area 3	< 0.001	ADHD	0.883
Medial IntraParietal Area	Area TF	< 0.001	ADHD	0.881
Ventral Visual Complex	Frontal Eye Fields	< 0.001	ADHD	0.881
Area 7m	Area TF	< 0.001	ADHD	0.879
Area 6m anterior	Eighth Visual Area	< 0.001	ADHD	0.879
Area Lateral IntraParietal dorsal	Ventral Visual Complex	< 0.001	ADHD	0.879
Area TA2	Posterior InferoTemporal complex	< 0.001	ADHD	0.878

Supplementary Table F20: Top connectivity features in high frequency range of ABIDE ASD prediction

Region 1	Region 2	Corrected p-value	Disorder/HC	Cohen's d
Dorsal Area 24d	Area PGs	< 0.001	ASD	6.950
Area p32	Area PGs	< 0.001	ASD	6.565
Ventral Area 6	Area 8 Anterior ventral	< 0.001	ASD	6.479
Area p32	Area 8 Anterior ventral	< 0.001	ASD	6.313
Area 9 Middle	Area 8 Anterior ventral	< 0.001	ASD	6.135
Area 9-46 dorsal	Area PGs	< 0.001	ASD	6.057
Area ventral 23 a+b	Area 8 Anterior ventral	< 0.001	ASD	6.041
Supplementary and Cingulate Eye Field	Area PGs	< 0.001	ASD	5.959
Area 31pd	Area 8 Anterior ventral	< 0.001	ASD	5.899
ParaHippocampal Area 3	Area 8Ad	< 0.001	ASD	5.819
Area 31 anterior	Area PGs	< 0.001	ASD	5.671
Orbital Frontal Complex	Area 47 medial	< 0.001	ASD	5.531
Area a24	Area 8 Anterior ventral	< 0.001	ASD	5.509
PreSubiculum	Area PGs	< 0.001	ASD	5.178
Area 31p ventral	Area 8 Anterior ventral	< 0.001	ASD	5.171
Area 23 dorsal	Area PGs	< 0.001	ASD	5.107
Area V3A	Area 47 medial	< 0.001	ASD	4.942
Area STSd anterior	Area PGs	< 0.001	ASD	4.881
Area TemporoParietoOccipital Junction 3	Area 8Ad	< 0.001	ASD	4.745
Area 46	Area 47 medial	0.001	ASD	4.683
Area IFSp	Area 47 medial	0.001	ASD	4.669
Area 10 rostral	Area 8 Anterior ventral	0.001	ASD	4.589

Continued on next page

Supplementary Table F20 – continued from previous page

Region 1	Region 2	Corrected p-value	Disorder/HC	Cohen's d
Area posterior 24	Area TE1 Middle	0.001	ASD	4.574
Area posterior 24	Area 8 Anterior ventral	0.001	ASD	4.550
Primary Visual Cortex	Area 47 medial	0.001	ASD	4.533
Area Posterior 24 prime	Area 47 medial	0.001	ASD	4.512
Premotor Eye Field	Area 47 medial	0.001	ASD	4.507
Ventral Area 6	Area PGs	0.001	ASD	4.502
Inferior 6-8 Transitional Area	Area 47 medial	0.001	ASD	4.456
PreSubiculum	Area 8 Anterior ventral	< 0.001	ASD	4.430
Area 9-46 dorsal	Area 8 Anterior ventral	< 0.001	ASD	4.377
VentroMedial Visual Area 1	Area 47 medial	0.001	ASD	4.365
Area 33 prime	Area 47 medial	0.001	ASD	4.293
Second Visual Area	Area 47 medial	0.001	ASD	4.274
Para-Insular Area	Area 8 Anterior ventral	0.001	ASD	4.227
ParaHippocampal Area 3	Area 8 Anterior ventral	0.001	ASD	4.222
Area PFm Complex	Area 8 Anterior ventral	0.001	ASD	4.222
Third Visual Area	Area 47 medial	0.001	ASD	4.206
Area Lateral Occipital 3	Area 47 medial	0.001	ASD	4.196
Area PGi	Area 8 Anterior ventral	0.001	ASD	4.193
Area p32 prime	Area PGs	0.001	ASD	4.178
Area 33 prime	Area 8 Anterior ventral	0.001	ASD	4.176
Superior Frontal Language Area	Area 8 Anterior ventral	< 0.001	ASD	4.176
Supplementary and Cingulate Eye Field	Area 8 Anterior ventral	0.001	ASD	4.166
Middle Insular Area	Area PGs	0.001	ASD	4.161
Area dorsal 32	Area 8 Anterior ventral	< 0.001	ASD	4.079
Area anterior 32 prime	Area 8 Anterior ventral	0.001	ASD	4.073

Continued on next page

Supplementary Table F20 – continued from previous page

Region 1	Region 2	Corrected p-value	Disorder/HC	Cohen's d
Area posterior 24	Area 47 medial	0.001	ASD	4.065
Area Lateral IntraParietal ventral	Area 47 medial	0.002	ASD	4.046
Area IFJp	Area 47 medial	0.001	ASD	4.034
Anterior 24 prime	Area 47 medial	0.002	ASD	4.026
Inferior 6-8 Transitional Area	Area TE1 Middle	0.002	ASD	4.011
Area 11 lateral	Area 47 medial	0.002	ASD	3.987
ParaHippocampal Area 3	Area 47l (47 lateral)	0.001	ASD	3.980
Area IntraParietal 1	Area 8 Anterior ventral	0.002	ASD	3.980
Superior 6-8 Transitional Area	Area TE1 Middle	0.001	ASD	3.968
Area PH	Area 47 medial	< 0.001	ASD	3.963
Area Lateral Occipital 2	Area 8 Anterior ventral	0.001	ASD	3.956
Eighth Visual Area	Inferior 6-8 Transitional Area	0.002	ASD	3.952
Area 6 anterior	Area 47 medial	0.002	ASD	3.948
Para-Insular Area	Area 47 medial	0.002	ASD	3.918
Area s32	Area PGs	0.002	ASD	3.913
Area OP1-SII	Inferior 6-8 Transitional Area	0.002	ASD	3.897
Area a24	Area PGs	0.002	ASD	3.895
Area TE1 Middle	Area 8 Anterior ventral	0.001	ASD	3.895
Area Lateral Occipital 2	Area 47 medial	0.002	ASD	3.875
Area 6 medial anterior	Area TE1 Middle	0.002	ASD	3.866
Area dorsal 23 a+b	Area 8 Anterior ventral	0.002	ASD	3.858
Supplementary and Cingulate Eye Field	Area TE1 Middle	0.002	ASD	3.843
Area TemporoParietoOccipital Junction 2	Area 8 Anterior ventral	0.002	ASD	3.840
Area posterior 9-46 ventral	Area 47 medial	< 0.001	ASD	3.825

Continued on next page

Supplementary Table F20 – continued from previous page

Region 1	Region 2	Corrected p-value	Disorder/HC	Cohen's d
Piriform Cortex	Area 47 medial	0.002	ASD	3.804
Area Posterior Insular 1	Area 47 medial	0.002	ASD	3.800
Fourth Visual Area	Area 47 medial	0.002	ASD	3.798
Area a24	Dorsal area 6	0.002	ASD	3.789
Area anterior 10p	Area TE1 Middle	0.002	ASD	3.788
Anterior 24 prime	Area TE1 Middle	0.002	ASD	3.785
Visual area 3-B	Area 47 medial	0.002	ASD	3.757
Area s32	Dorsal area 6	0.002	ASD	3.752
Area TemporoParietoOccipital Junction 3	Area 8 Anterior ventral	0.002	ASD	3.744
RetroInsular Cortex	Area 8 Anterior ventral	0.002	ASD	3.736
Area 46	Area 8 Anterior ventral	< 0.001	ASD	3.731
Perirhinal Ectorhinal Cortex	Area 47 medial	0.002	ASD	3.731
Area p32 prime	Area 47 medial	0.002	ASD	3.720
Lateral Belt Complex	Area 47 medial	0.002	ASD	3.702
Anterior 24 prime	Area 8 Anterior ventral	0.002	ASD	3.698
Area OP1-SII	Primary Motor Cortex	0.002	ASD	3.694
Area 6 medial anterior	Superior 6-8 Transitional Area	0.002	ASD	3.693
Area Lateral IntraParietal dorsal	Medial Area 7P (posterior)	0.002	ASD	3.693
Area p32 prime	Area 8 Anterior ventral	0.002	ASD	3.682
Premotor Eye Field	Area 8 Anterior ventral	0.002	ASD	3.678
Entorhinal Cortex	Area 47 medial	0.003	ASD	3.654
Area 31 anterior	Area 8 Anterior ventral	0.002	ASD	3.629
Area 7m	Area 8 Anterior ventral	0.002	ASD	3.625
Area dorsal 32	Area TG dorsal	0.003	ASD	3.608
Area Posterior 24 prime	Area 8 Anterior ventral	0.002	ASD	3.602

Continued on next page

Supplementary Table F20 – continued from previous page

Region 1	Region 2	Corrected p-value	Disorder/HC	Cohen's d
Area IntraParietal 1	Medial Area 7P (posterior)	0.002	ASD	3.593
Area dorsal 23 a+b	Inferior 6-8 Transitional Area	0.003	ASD	3.579
Ventral Area 6	Area 47 medial	0.003	ASD	3.574
Area 31pd	Area PGs	0.001	ASD	3.556

Supplementary Table F21: Top connectivity features in low frequency range of ABIDE ASD prediction

Region 1	Region 2	Corrected p-value	Disorder/HC	Cohen's d
Area PHT	Area posterior 9-46 ventral	0.028	ASD	2.155
ParaBelt Complex	Area posterior 9-46 ventral	0.029	ASD	2.154
Auditory 5 Complex	Area posterior 9-46 ventral	0.030	ASD	2.123
Area 9 Posterior	Area posterior 9-46 ventral	0.030	ASD	2.122
Primary Sensory Cortex	Area posterior 9-46 ventral	0.031	ASD	2.116
Area PH	Area posterior 9-46 ventral	0.031	ASD	2.115
Area 3a	Area posterior 9-46 ventral	0.031	ASD	2.109
Area 6mp	Area posterior 9-46 ventral	0.032	ASD	2.099
Lateral Belt Complex	Area posterior 9-46 ventral	0.033	ASD	2.078
Area TA2	Area posterior 9-46 ventral	0.034	ASD	2.065
Area TE2 posterior	Area posterior 9-46 ventral	0.034	ASD	2.057
Area V3A	Area posterior 9-46 ventral	0.034	ASD	2.057
Area PFm Complex	Area posterior 9-46 ventral	0.034	ASD	2.053
Area Lateral Occipital 2	Area posterior 9-46 ventral	0.035	ASD	2.046
Dorsal area 6	Area posterior 9-46 ventral	0.035	ASD	2.045
VentroMedial Visual Area 1	Area posterior 9-46 ventral	0.035	ASD	2.039
ParaHippocampal Area 3	Area posterior 9-46 ventral	0.036	ASD	2.038
Area IFSp	Area posterior 9-46 ventral	0.036	ASD	2.037
Primary Auditory Cortex	Area posterior 9-46 ventral	0.036	ASD	2.032
Ventral Visual Complex	Area posterior 9-46 ventral	0.037	ASD	2.023
Area 1	Area posterior 9-46 ventral	0.036	ASD	2.018
Area PGs	Area posterior 9-46 ventral	0.037	ASD	2.009
Area IntraParietal 2	Area posterior 9-46 ventral	0.037	ASD	2.007

Continued on next page

Supplementary Table F21 – continued from previous page

Region 1	Region 2	Corrected p-value	Disorder/HC	Cohen's d
Area TemporoParietoOccipital Junction 1	Area posterior 9-46 ventral	0.037	ASD	2.004
Primary Motor Cortex	Area posterior 9-46 ventral	0.038	ASD	2.001
ParaHippocampal Area 1	Area posterior 9-46 ventral	0.039	ASD	1.999
Auditory 4 Complex	Area posterior 9-46 ventral	0.039	ASD	1.993
Area 31a	Area posterior 9-46 ventral	0.039	ASD	1.987
Area TE1 posterior	Area posterior 9-46 ventral	0.039	ASD	1.985
Superior Temporal Visual Area	Area posterior 9-46 ventral	0.039	ASD	1.980
Area 25	Area posterior 9-46 ventral	0.040	ASD	1.978
Area V6A	Area posterior 9-46 ventral	0.039	ASD	1.977
Area OP2-3-VS	Area posterior 9-46 ventral	0.040	ASD	1.975
Ventral Area 24d	Area posterior 9-46 ventral	0.041	ASD	1.975
Area 2	Area posterior 9-46 ventral	0.040	ASD	1.963
ProStriate Area	Area posterior 9-46 ventral	0.041	ASD	1.960
RetroInsular Cortex	Area posterior 9-46 ventral	0.041	ASD	1.960
Area 9 anterior	Area posterior 9-46 ventral	0.041	ASD	1.954
VentroMedial Visual Area 3	Area posterior 9-46 ventral	0.042	ASD	1.953
ParaHippocampal Area 2	Area posterior 9-46 ventral	0.042	ASD	1.947
Area anterior 9-46 ventral	Area posterior 9-46 ventral	0.043	ASD	1.941
Medial Belt Complex	Area posterior 9-46 ventral	0.043	ASD	1.940
Insular Granular Complex	Area posterior 9-46 ventral	0.043	ASD	1.936
Eighth Visual Area	Area posterior 9-46 ventral	0.044	ASD	1.933
Superior Frontal Language Area	Area posterior 9-46 ventral	0.044	ASD	1.931
Area TemporoParietoOccipital Junction 3	Area posterior 9-46 ventral	0.044	ASD	1.921
Area 43	Area posterior 9-46 ventral	0.044	ASD	1.920

Continued on next page

Supplementary Table F21 – continued from previous page

Region 1	Region 2	Corrected p-value	Disorder/HC	Cohen's d
Posterior InferoTemporal complex	Area posterior 9-46 ventral	0.045	ASD	1.915
Area 7PC	Area posterior 9-46 ventral	0.045	ASD	1.913
Area STSv posterior	Area posterior 9-46 ventral	0.044	ASD	1.912
Area V3B	Area posterior 9-46 ventral	0.046	ASD	1.908
Area Lateral IntraParietal dorsal	Area posterior 9-46 ventral	0.045	ASD	1.905
Area Lateral Occipital 1	Area posterior 9-46 ventral	0.046	ASD	1.904
Area Posterior Insular 1	Area posterior 9-46 ventral	0.046	ASD	1.900
Dorsal Transitional Visual Area	Area posterior 9-46 ventral	0.046	ASD	1.900
Fusiform Face Complex	Area posterior 9-46 ventral	0.047	ASD	1.890
Second Visual Area	Area posterior 9-46 ventral	0.048	ASD	1.887
PeriSylvian Language Area	Area posterior 9-46 ventral	0.047	ASD	1.887
Area s32	Area posterior 9-46 ventral	0.047	ASD	1.885
Area 46	Area posterior 9-46 ventral	0.047	ASD	1.884
Hippocampus	Area posterior 9-46 ventral	0.048	ASD	1.880
VentroMedial Visual Area 2	Area posterior 9-46 ventral	0.048	ASD	1.879
Area 8Av	Area posterior 9-46 ventral	0.048	ASD	1.877
Area OP4-PV	Area posterior 9-46 ventral	0.048	ASD	1.877
Posterior Insular Area 2	Area posterior 9-46 ventral	0.048	ASD	1.876
Area TemporoParietoOccipital Junction 2	Area posterior 9-46 ventral	0.047	ASD	1.876
Area 55b	Area posterior 9-46 ventral	0.048	ASD	1.876
Area 23d	Area posterior 9-46 ventral	0.048	ASD	1.874
PreSubiculum	Area posterior 9-46 ventral	0.048	ASD	1.871
Anterior IntraParietal Area	Area posterior 9-46 ventral	0.048	ASD	1.870
Area PFcm	Area posterior 9-46 ventral	0.049	ASD	1.869
Ventral Area 6	Area posterior 9-46 ventral	0.049	ASD	1.867

Continued on next page

Supplementary Table F21 – continued from previous page

Region 1	Region 2	Corrected p-value	Disorder/HC	Cohen's d
Area 33 prime	Area posterior 9-46 ventral	0.049	ASD	1.866
Area STSd posterior	Area posterior 9-46 ventral	0.048	ASD	1.865
Parieto-Occipital Sulcus Area 1	Area posterior 9-46 ventral	0.049	ASD	1.862
Seventh Visual Area	Area posterior 9-46 ventral	0.050	ASD	1.860
Area OP1-SII	Area posterior 9-46 ventral	0.049	ASD	1.860
Area STSd posterior	Area Lateral IntraParietal dorsal	0.049	ASD	1.838

Supplementary Table F22: Top connectivity features in ultralow frequency range of ABIDE ASD prediction

Region 1	Region 2	Corrected p-value	Disorder/HC	Cohen's d
Medial Belt Complex	Area 7PC	0.002	HC	3.728
Area TA2 (temporal region A, area 2)	Area 7PC	0.005	HC	3.157
ParaBelt Complex	Area Frontal Opercular 5	0.005	HC	3.119
Dorsal area 6	Area Frontal Opercular 5	0.009	HC	2.781
ParaHippocampal Area 1	Area 7PC	0.009	HC	2.752
Auditory 4 Complex	Area 7PC	0.011	HC	2.739
ParaHippocampal Area 1	Area posterior 9-46 ventral	0.010	HC	2.729
Auditory 4 Complex	Area Frontal Opercular 5	0.011	HC	2.696
Area PH	Area Frontal Opercular 5	0.004	HC	2.570
Superior 6-8 Transitional Area	Area 7PC	0.013	HC	2.551
Posterior Insular Area 2	Area Frontal Opercular 5	0.014	HC	2.546
Medial Belt Complex	Area Lateral IntraParietal dorsal	0.005	HC	2.541
ParaHippocampal Area 1	Area IFJa	0.014	HC	2.520
Medial Belt Complex	Area posterior 9-46 ventral	0.014	HC	2.518
Area anterior 9-46 ventral	Area 7PC	0.014	HC	2.515
Area OP2-3-VS (Ventral-Superior part of 2-3 area of Parietal Operculum)	Area Frontal Opercular 5	0.014	HC	2.503
Medial Belt Complex	Area IFJa	0.017	HC	2.444
Area 8B Lateral	Area 7PC	0.006	HC	2.440
Area 6 medial anterior	Area Lateral IntraParietal dorsal	0.005	HC	2.436
ParaBelt Complex	Area 7PC	0.017	HC	2.433
Middle Temporal Area	Area 7PC	0.017	HC	2.402
Area 52	Area Lateral IntraParietal dorsal	0.006	HC	2.398
Area 46	Area Frontal Opercular 5	0.018	HC	2.394

Continued on next page

Supplementary Table F22 – continued from previous page

Region 1	Region 2	Corrected p-value	Disorder/HC	Cohen's d
Medial Belt Complex	Frontal Opercular Area 2	0.018	HC	2.379
Dorsal area 6	Area Lateral IntraParietal dorsal	0.006	HC	2.374
Area 6 medial posterior	Area Lateral IntraParietal dorsal	0.019	HC	2.364
Posterior Insular Area 2	Area 7PC	0.019	HC	2.357
Area OP4-PV (Posterior-Ventral part of area 4 of Parietal Operculum)	Area Frontal Opercular 5	0.020	HC	2.335
Inferior 6-8 Transitional Area	Area Frontal Opercular 5	0.021	HC	2.328
Frontal Opercular Area 1	Area Lateral IntraParietal dorsal	0.006	HC	2.319
Area posterior 10p	Area 7PC	0.021	HC	2.310
Primary Auditory Cortex	Area 7PC	0.023	HC	2.308
Dorsal area 6	Area 7PC	0.021	HC	2.305
Anterior Agranular Insula Complex	Area Frontal Opercular 5	0.023	HC	2.290
ParaHippocampal Area 1	Area Lateral IntraParietal dorsal	0.007	HC	2.287
Auditory 4 Complex	Area IFJa	0.022	HC	2.276
Auditory 4 Complex	Area posterior 9-46 ventral	0.024	HC	2.267
Area IFJa	Area Frontal Opercular 5	0.022	HC	2.265
Area 9 Middle	Area PGs	0.022	HC	2.264
Area posterior 9-46 ventral	Area Frontal Opercular 5	0.024	HC	2.256
Area anterior 9-46 ventral	Area Frontal Opercular 5	0.023	HC	2.255
Area PF Opercular	Area Frontal Opercular 5	0.023	HC	2.254
Frontal Opercular Area 1	Area 7PC	0.023	HC	2.248
PreSubiculum	Area PGs	0.023	HC	2.247
Superior 6-8 Transitional Area	Area Lateral IntraParietal dorsal	0.024	HC	2.241
Area TA2 (temporal region A, area 2)	Area Lateral IntraParietal dorsal	0.023	HC	2.241
Area OP1-SII	Area Frontal Opercular 5	0.024	HC	2.229
Area s32	Area 7PC	0.024	HC	2.228

Continued on next page

Supplementary Table F22 – continued from previous page

Region 1	Region 2	Corrected p-value	Disorder/HC	Cohen's d
Medial Belt Complex	Area Frontal Opercular 5	0.008	HC	2.226
Area PH	Area IFJa	0.024	HC	2.224
Area Posterior Insular 1	Area Lateral IntraParietal dorsal	0.024	HC	2.215
VentroMedial Visual Area 1	Area Frontal Opercular 5	0.025	HC	2.213
Area 33 prime	Area Frontal Opercular 5	0.025	HC	2.211
Area 43	Area IFJa	0.026	HC	2.209
Area OP2-3-VS (Ventral-Superior part of 2-3 area of Parietal Operculum)	Area Lateral IntraParietal dorsal	0.025	HC	2.206
Frontal Opercular Area 1	Area Frontal Opercular 5	0.025	HC	2.205
Piriform Cortex	Area Lateral IntraParietal dorsal	0.009	HC	2.187
Area 9 anterior	Area PGs	0.026	HC	2.183
Area 8B Lateral	Area PGs	0.026	HC	2.183
Area PF Complex	Area Frontal Opercular 5	0.027	HC	2.179
Anterior Agranular Insula Complex	Area posterior 9-46 ventral	0.027	HC	2.176
Area 1	Area Frontal Opercular 5	0.027	HC	2.173
Premotor Eye Field	Area Frontal Opercular 5	0.027	HC	2.173
ParaHippocampal Area 1	Area Frontal Opercular 5	0.027	HC	2.172
Area PFt	Area Frontal Opercular 5	0.027	HC	2.169
Area 13 lateral	Area Frontal Opercular 5	0.027	HC	2.163
Rostral Area 6	Area 7PC	0.028	HC	2.159
Anterior Agranular Insula Complex	Area 7PC	0.029	HC	2.143
Area 6 medial posterior	Area PGs	0.028	HC	2.139
Area 43	Area Frontal Opercular 5	0.028	HC	2.138
Area OP4-PV (Posterior-Ventral part of area 4 of Parietal Operculum)	Area Lateral IntraParietal dorsal	0.028	HC	2.138
Posterior Insular Area 2	Area posterior 9-46 ventral	0.029	HC	2.128

Continued on next page

Supplementary Table F22 – continued from previous page

Region 1	Region 2	Corrected p-value	Disorder/HC	Cohen's d
ParaHippocampal Area 1	Sixth Visual Area	0.030	HC	2.114
Parieto-Occipital Sulcus Area 1	Area Lateral IntraParietal dorsal	0.009	HC	2.111
Area posterior 10p	Area Frontal Opercular 5	0.031	HC	2.108
Ventral Area 6	Area Frontal Opercular 5	0.030	HC	2.106
Area STSd anterior	Area Lateral IntraParietal dorsal	0.009	HC	2.100
Area anterior 9-46 ventral	Area Lateral IntraParietal dorsal	0.031	HC	2.093
Area Posterior Insular 1	Area PGs	0.031	HC	2.093
Rostral Area 6	Area Frontal Opercular 5	0.010	HC	2.091
Area FST	Area Frontal Opercular 5	0.031	HC	2.085
Area Superior temporal sulcus ventral anterior	Area 7PC	0.031	HC	2.081
Area Posterior Insular 1	Area posterior 9-46 ventral	0.032	HC	2.076
Area TE1 Middle	Area 7PC	0.032	HC	2.070
Area 6 medial posterior	Area 7PC	0.032	HC	2.069
Area Posterior Insular 1	Area 7PC	0.032	HC	2.067
Area Posterior Insular 1	Area Frontal Opercular 5	0.033	HC	2.063
Area TA2 (temporal region A, area 2)	Area PGs	0.032	HC	2.062
PreSubiculum	Area Lateral IntraParietal dorsal	0.011	HC	2.055
Area 43	Area 7PC	0.033	HC	2.048
ParaHippocampal Area 2	Area 7PC	0.034	HC	2.045
Inferior 6-8 Transitional Area	Area Lateral IntraParietal dorsal	0.034	HC	2.044
ParaHippocampal Area 3	Area Lateral IntraParietal dorsal	0.012	HC	2.043
Area 10 rostral	Area PGs	0.034	HC	2.041
ParaBelt Complex	Area Lateral IntraParietal dorsal	0.034	HC	2.041
Medial Superior Temporal Area	Area Frontal Opercular 5	0.034	HC	2.041
Superior 6-8 Transitional Area	Area PGs	0.034	HC	2.040

Continued on next page

Supplementary Table F22 – continued from previous page

Region 1	Region 2	Corrected p-value	Disorder/HC	Cohen's d
Entorhinal Cortex	Area Lateral IntraParietal dorsal	0.034	HC	2.037
VentroMedial Visual Area 1	Area IFJa	0.034	HC	2.036
Area Lateral Occipital 3	Area Lateral IntraParietal dorsal	0.012	HC	2.033

References

- [1] Taghia, J., Cai, W., Ryali, S., Kochalka, J., Nicholas, J., Chen, T., Menon, V.: Uncovering hidden brain state dynamics that regulate performance and decision-making during cognition. *Nature communications* **9**(1), 2505 (2018)
- [2] He, B.J., Zempel, J.M., Snyder, A.Z., Raichle, M.E.: The temporal structures and functional significance of scale-free brain activity. *Neuron* **66**(3), 353–369 (2010)
- [3] Sendi, M.S., Fu, Z., Harnett, N.G., Rooij, S.J., Vergara, V., Pizzagalli, D.A., Daskalakis, N.P., House, S.L., Beaudoin, F.L., An, X., et al.: Brain dynamics reflecting an intra-network brain state are associated with increased post-traumatic stress symptoms in the early aftermath of trauma. *Nature Mental Health*, 1–14 (2025)
- [4] Breakspear, M.: Dynamic models of large-scale brain activity. *Nature neuroscience* **20**(3), 340–352 (2017)
- [5] Kan, X., Dai, W., Cui, H., Zhang, Z., Guo, Y., Yang, C.: Brain network transformer. *Advances in Neural Information Processing Systems* **35**, 25586–25599 (2022)
- [6] Bedel, H.A., Sivgin, I., Dalmaz, O., Dar, S.U., Çukur, T.: Bolt: Fused window transformers for fmri time series analysis. *Medical image analysis* **88**, 102841 (2023)
- [7] Wang, C., Subramaniam, V., Yaari, A.U., Kreiman, G., Katz, B., Cases, I., Barbu, A.: Brainbert: Self-supervised representation learning for intracranial recordings. *arXiv preprint arXiv:2302.14367* (2023)
- [8] Ortega Caro, J., Oliveira Fonseca, A.H., Averill, C., Rizvi, S.A., Rosati, M., Cross, J.L., Mittal, P., Zappala, E., Levine, D., Dhodapkar, R.M., et al.: Brainlm: A foundation model for brain activity recordings. *bioRxiv*, 2023–09 (2023)
- [9] Radulescu, A.R., Rubin, D., Strey, H.H., Mujica-Parodi, L.R.: Power spectrum scale invariance identifies prefrontal dysregulation in paranoid schizophrenia. *Human brain mapping* **33**(7), 1582–1593 (2012)
- [10] Stylianou, O., Kaposzta, Z., Czoch, A., Stefanovski, L., Yabluchanskiy, A., Racz, F.S., Ritter, P., Eke, A., Mukli, P.: Scale-free functional brain networks exhibit increased connectivity, are more integrated and less segregated in patients with parkinson’s disease following dopaminergic treatment. *Fractal and fractional* **6**(12), 737 (2022)
- [11] Smit, D.J., Geus, E.J., Nieuwenhuijzen, M.E., Beijsterveldt, C.E., Baal, G.C.M., Mansvelder, H.D., Boomsma, D.I., Linkenkaer-Hansen, K.: Scale-free modulation of resting-state neuronal oscillations reflects prolonged brain maturation in

- humans. *Journal of Neuroscience* **31**(37), 13128–13136 (2011)
- [12] Tagliazucchi, E., Wegner, F., Morzelewski, A., Brodbeck, V., Jahnke, K., Laufs, H.: Breakdown of long-range temporal dependence in default mode and attention networks during deep sleep. *Proceedings of the National Academy of Sciences* **110**(38), 15419–15424 (2013)
- [13] Tolkunov, D., Rubin, D., Mujica-Parodi, L.R.: Power spectrum scale invariance quantifies limbic dysregulation in trait anxious adults using fmri: adapting methods optimized for characterizing autonomic dysregulation to neural dynamic time series. *Neuroimage* **50**(1), 72–80 (2010)
- [14] Maxim, V., Şendur, L., Fadili, J., Suckling, J., Gould, R., Howard, R., Bullmore, E.: Fractional gaussian noise, functional mri and alzheimer’s disease. *Neuroimage* **25**(1), 141–158 (2005)
- [15] Stanley, H.E., Meakin, P.: Multifractal phenomena in physics and chemistry. *Nature* **335**(6189), 405–409 (1988)
- [16] Falconer, K.: *Fractal Geometry: Mathematical Foundations and Applications*. John Wiley & Sons, ??? (2013)
- [17] Salat, H., Murcio, R., Arcaute, E.: Multifractal methodology. *Physica A: Statistical Mechanics and its Applications* **473**, 467–487 (2017)
- [18] Guidolin, D., Tortorella, C., De Caro, R., Agnati, L.F.: In: Di Ieva, A. (ed.) *A Self-Similarity Logic May Shape the Organization of the Nervous System*, pp. 203–225. Springer, Cham (2024). https://doi.org/10.1007/978-3-031-47606-8_10 . https://doi.org/10.1007/978-3-031-47606-8_10
- [19] Ciuciu, P., Abry, P., Rabrait, C., Wendt, H.: Log wavelet leaders cumulant based multifractal analysis of evi fmri time series: evidence of scaling in ongoing and evoked brain activity. *IEEE Journal of Selected Topics in Signal Processing* **2**(6), 929–943 (2008)
- [20] Miller, K.J., Sorensen, L.B., Ojemann, J.G., Den Nijs, M.: Power-law scaling in the brain surface electric potential. *PLoS computational biology* **5**(12), 1000609 (2009)
- [21] Achard, S., Salvador, R., Whitcher, B., Suckling, J., Bullmore, E.: A resilient, low-frequency, small-world human brain functional network with highly connected association cortical hubs. *Journal of Neuroscience* **26**(1), 63–72 (2006)
- [22] Sasai, S., Koike, T., Sugawara, S.K., Hamano, Y.H., Sumiya, M., Okazaki, S., Takahashi, H.K., Taga, G., Sadato, N.: Frequency-specific task modulation of human brain functional networks: A fast fmri study. *NeuroImage* **224**, 117375 (2021)

- [23] Hagler Jr, D.J., Hatton, S., Cornejo, M.D., Makowski, C., Fair, D.A., Dick, A.S., Sutherland, M.T., Casey, B., Barch, D.M., Harms, M.P., *et al.*: Image processing and analysis methods for the adolescent brain cognitive development study. *Neuroimage* **202**, 116091 (2019)
- [24] Marek, S., Tervo-Clemmens, B., Calabro, F.J., Montez, D.F., Kay, B.P., Hatoum, A.S., Donohue, M.R., Foran, W., Miller, R.L., Hendrickson, T.J., *et al.*: Reproducible brain-wide association studies require thousands of individuals. *Nature* **603**(7902), 654–660 (2022)
- [25] Ingalhalikar, M., Shinde, S., Karmarkar, A., Rajan, A., Rangaprakash, D., Deshpande, G.: Functional connectivity-based prediction of autism on site harmonized abide dataset. *IEEE transactions on biomedical engineering* **68**(12), 3628–3637 (2021)
- [26] Esteban, O., Markiewicz, C.J., Blair, R.W., Moodie, C.A., Isik, A.I., Erramuzpe, A., Kent, J.D., Goncalves, M., DuPre, E., Snyder, M., *et al.*: fmriprep: a robust preprocessing pipeline for functional mri. *Nature methods* **16**(1), 111–116 (2019)
- [27] Behzadi, Y., Restom, K., Liau, J., Liu, T.T.: A component based noise correction method (compcor) for bold and perfusion based fmri. *Neuroimage* **37**(1), 90–101 (2007)
- [28] Glasser, M.F., Coalson, T.S., Robinson, E.C., Hacker, C.D., Harwell, J., Yacoub, E., Ugurbil, K., Andersson, J., Beckmann, C.F., Jenkinson, M., *et al.*: A multi-modal parcellation of human cerebral cortex. *Nature* **536**(7615), 171–178 (2016)
- [29] Schaefer, A., Kong, R., Gordon, E.M., Laumann, T.O., Zuo, X.-N., Holmes, A.J., Eickhoff, S.B., Yeo, B.T.: Local-global parcellation of the human cerebral cortex from intrinsic functional connectivity mri. *Cerebral cortex* **28**(9), 3095–3114 (2018)
- [30] Cordova, M.M., Antovich, D.M., Ryabinin, P., Neighbor, C., Mooney, M.A., Dieckmann, N.F., Miranda-Dominguez, O., Nagel, B.J., Fair, D.A., Nigg, J.T.: Attention-deficit/hyperactivity disorder: restricted phenotypes prevalence, comorbidity, and polygenic risk sensitivity in the abcd baseline cohort. *Journal of the American Academy of Child & Adolescent Psychiatry* **61**(10), 1273–1284 (2022)
- [31] Martin, C.H., Peng, T., Mahoney, M.W.: Predicting trends in the quality of state-of-the-art neural networks without access to training or testing data. *Nature Communications* **12**(1), 4122 (2021)
- [32] Bentkamp, L., Lalescu, C.C., Wilczek, M.: Persistent accelerations disentangle lagrangian turbulence. *Nature Communications* **10**(1), 3550 (2019)
- [33] Li, T., Biferale, L., Bonaccorso, F., Scarpolini, M.A., Buzzicotti, M.: Synthetic

- lagrangian turbulence by generative diffusion models. *Nature Machine Intelligence* **6**(4), 393–403 (2024)
- [34] Kajimura, S., Margulies, D., Smallwood, J.: Frequency-specific brain network architecture in resting-state fmri. *Scientific Reports* **13**(1), 2964 (2023)
- [35] Zuo, X.-N., Di Martino, A., Kelly, C., Shehzad, Z.E., Gee, D.G., Klein, D.F., Castellanos, F.X., Biswal, B.B., Milham, M.P.: The oscillating brain: complex and reliable. *Neuroimage* **49**(2), 1432–1445 (2010)
- [36] He, B.J.: Scale-free brain activity: past, present, and future. *Trends in cognitive sciences* **18**(9), 480–487 (2014)
- [37] Yu, Y., Qiu, Y., Li, G., Zhang, K., Bo, B., Pei, M., Ye, J., Thompson, G.J., Cang, J., Fang, F., *et al.*: Sleep fmri with simultaneous electrophysiology at 9.4 t in male mice. *Nature communications* **14**(1), 1651 (2023)
- [38] Shim, W.H., Baek, K., Kim, J.K., Chae, Y., Suh, J.-Y., Rosen, B.R., Jeong, J., Kim, Y.R.: Frequency distribution of causal connectivity in rat sensorimotor network: resting-state fmri analyses. *Journal of Neurophysiology* **109**(1), 238–248 (2013)
- [39] Devlin, J., Chang, M.-W., Lee, K., Toutanova, K.: Bert: Pre-training of deep bidirectional transformers for language understanding. *arXiv preprint arXiv:1810.04805* (2018)
- [40] Baevski, A., Zhou, Y., Mohamed, A., Auli, M.: wav2vec 2.0: A framework for self-supervised learning of speech representations. *Advances in neural information processing systems* **33**, 12449–12460 (2020)
- [41] Mohanty, R., Sethares, W.A., Nair, V.A., Prabhakaran, V.: Rethinking measures of functional connectivity via feature extraction. *Scientific reports* **10**(1), 1298 (2020)
- [42] Vaswani, A.: Attention is all you need. *Advances in Neural Information Processing Systems* (2017)
- [43] Selvaraju, R.R., Cogswell, M., Das, A., Vedantam, R., Parikh, D., Batra, D.: Grad-cam: Visual explanations from deep networks via gradient-based localization. In: *Proceedings of the IEEE International Conference on Computer Vision*, pp. 618–626 (2017)
- [44] Cohen, J.: *Statistical Power Analysis for the Behavioral Sciences*. routledge, ??? (2013)
- [45] Chen, T., He, T., Benesty, M., Khotilovich, V., Tang, Y., Cho, H., Chen, K., Mitchell, R., Cano, I., Zhou, T., *et al.*: Xgboost: extreme gradient boosting. *R*

package version 0.4-2 **1**(4), 1–4 (2015)

- [46] Suckling, J., Wink, A.M., Bernard, F.A., Barnes, A., Bullmore, E.: Endogenous multifractal brain dynamics are modulated by age, cholinergic blockade and cognitive performance. *Journal of neuroscience methods* **174**(2), 292–300 (2008)
- [47] La Rocca, D., Zilber, N., Abry, P., Wassenhove, V., Ciuciu, P.: Self-similarity and multifractality in human brain activity: A wavelet-based analysis of scale-free brain dynamics. *Journal of neuroscience methods* **309**, 175–187 (2018)
- [48] Guan, S., Wan, D., Yang, Y., Biswal, B.: Sources of multifractality of the brain rs-fmri signal. *Chaos, Solitons & Fractals* **160**, 112222 (2022)
- [49] Heuvel, M.P., Stam, C.J., Boersma, M., Pol, H.H.: Small-world and scale-free organization of voxel-based resting-state functional connectivity in the human brain. *Neuroimage* **43**(3), 528–539 (2008)
- [50] França, L.G.S., Miranda, J.G.V., Leite, M., Sharma, N.K., Walker, M.C., Lemieux, L., Wang, Y.: Fractal and multifractal properties of electrographic recordings of human brain activity: toward its use as a signal feature for machine learning in clinical applications. *Frontiers in physiology* **9**, 1767 (2018)
- [51] Telesford, Q.K., Simpson, S.L., Burdette, J.H., Hayasaka, S., Laurienti, P.J.: The brain as a complex system: using network science as a tool for understanding the brain. *Brain connectivity* **1**(4), 295–308 (2011)
- [52] Sporns, O.: The human connectome: a complex network. *Annals of the new York Academy of Sciences* **1224**(1), 109–125 (2011)
- [53] Bullmore, E., Long, C., Suckling, J., Fadili, J., Calvert, G., Zelaya, F., Carpenter, T.A., Brammer, M.: Colored noise and computational inference in neurophysiological (fmri) time series analysis: resampling methods in time and wavelet domains. *Human brain mapping* **12**(2), 61–78 (2001)
- [54] Fox, M.D., Raichle, M.E.: Spontaneous fluctuations in brain activity observed with functional magnetic resonance imaging. *Nature reviews neuroscience* **8**(9), 700–711 (2007)
- [55] He, B.J.: Scale-free properties of the functional magnetic resonance imaging signal during rest and task. *Journal of Neuroscience* **31**(39), 13786–13795 (2011)
- [56] Mandelbrot, B.B., Van Ness, J.W.: Fractional brownian motions, fractional noises and applications. *SIAM review* **10**(4), 422–437 (1968)
- [57] Eke, A., Herman, P., Kocsis, L., Kozak, L.: Fractal characterization of complexity in temporal physiological signals. *Physiological measurement* **23**(1), 1 (2002)

- [58] Cha, J., DeDora, D., Nedic, S., Ide, J., Greenberg, T., Hajcak, G., Mujica-Parodi, L.R.: Clinically anxious individuals show disrupted feedback between inferior frontal gyrus and prefrontal-limbic control circuit. *Journal of Neuroscience* **36**(17), 4708–4718 (2016)
- [59] Tu, W., Liao, Q., Zhou, S., Peng, X., Ma, C., Liu, Z., Liu, X., Cai, Z., He, K.: Rare: Robust masked graph autoencoder. *IEEE Transactions on Knowledge and Data Engineering* (2023)
- [60] Liu, C., Wang, Y., Zhan, Y., Ma, X., Tao, D., Wu, J., Hu, W.: Where to mask: Structure-guided masking for graph masked autoencoders. *arXiv preprint arXiv:2404.15806* (2024)
- [61] Estrada, E., Hatano, N.: Communicability in complex networks. *Physical Review E* **77**(3), 036111 (2008)
- [62] Harush, U., Barzel, B.: Dynamic patterns of information flow in complex networks. *Nature communications* **8**(1), 2181 (2017)
- [63] Bush, G.: Attention-deficit/hyperactivity disorder and attention networks. *Neuropsychopharmacology* **35**(1), 278–300 (2010)
- [64] Lenz, D., Krauel, K., Flechtner, H.-H., Schadow, J., Hinrichs, H., Herrmann, C.S.: Altered evoked gamma-band responses reveal impaired early visual processing in adhd children. *Neuropsychologia* **48**(7), 1985–1993 (2010)
- [65] Skodzik, T., Holling, H., Pedersen, A.: Long-term memory performance in adult adhd: A meta-analysis. *Journal of attention disorders* **21**(4), 267–283 (2017)
- [66] Christiansen, H., Hirsch, O., Albrecht, B., Chavanon, M.-L.: Attention-deficit/hyperactivity disorder (adhd) and emotion regulation over the life span. *Current psychiatry reports* **21**, 1–11 (2019)
- [67] Ghanizadeh, A.: Sensory processing problems in children with adhd, a systematic review. *Psychiatry investigation* **8**(2), 89 (2010)
- [68] Bunford, N., Evans, S.W., Wymbs, F.: Adhd and emotion dysregulation among children and adolescents. *Clinical child and family psychology review* **18**, 185–217 (2015)
- [69] Chita-Tegmark, M.: Social attention in asd: A review and meta-analysis of eye-tracking studies. *Research in developmental disabilities* **48**, 79–93 (2016)
- [70] Solomon, M., Ozonoff, S.J., Cummings, N., Carter, C.S.: Cognitive control in autism spectrum disorders. *International Journal of Developmental Neuroscience* **26**(2), 239–247 (2008)
- [71] Patil, O., Kaple, M., Kaple, M.N.: Sensory processing differences in individuals

with autism spectrum disorder: a narrative review of underlying mechanisms and sensory-based interventions. *Cureus* **15**(10) (2023)

- [72] Peiker, I., David, N., Schneider, T.R., Nolte, G., Schöttle, D., Engel, A.K.: Perceptual integration deficits in autism spectrum disorders are associated with reduced interhemispheric gamma-band coherence. *Journal of Neuroscience* **35**(50), 16352–16361 (2015)
- [73] DuBois, D., Ameis, S.H., Lai, M.-C., Casanova, M.F., Desarkar, P.: Interoception in autism spectrum disorder: A review. *International journal of developmental neuroscience* **52**, 104–111 (2016)
- [74] Booth, R.D., Happé, F.G.: Evidence of reduced global processing in autism spectrum disorder. *Journal of autism and developmental disorders* **48**, 1397–1408 (2018)